

Summer 2019

Optical and Electrical Analysis of ZnO/ZnTe Micropillar Solar Cells

Sadia Binte Sohid

Bucknell University, sbs019@bucknell.edu

Follow this and additional works at: https://digitalcommons.bucknell.edu/masters_theses

 Part of the [Electromagnetics and Photonics Commons](#), [Electronic Devices and Semiconductor Manufacturing Commons](#), and the [Power and Energy Commons](#)

Recommended Citation

Sohid, Sadia Binte, "Optical and Electrical Analysis of ZnO/ZnTe Micropillar Solar Cells" (2019). *Master's Theses*. 223.
https://digitalcommons.bucknell.edu/masters_theses/223

This Masters Thesis is brought to you for free and open access by the Student Theses at Bucknell Digital Commons. It has been accepted for inclusion in Master's Theses by an authorized administrator of Bucknell Digital Commons. For more information, please contact dcadmin@bucknell.edu.

I, Sadia Binte Sohid, do grant permission for my thesis to be copied.

OPTICAL AND ELECTRICAL ANALYSIS OF ZnO/
ZnTe MICROPILLAR SOLAR CELLS

by

Sadia Binte Sohid

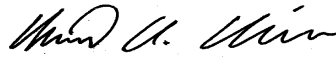
A Thesis

Presented to the Faculty of
Bucknell University
In Partial Fulfillment of the Requirements for the Degree of
Master of Science in Electrical Engineering

Approved:



Adviser: Dr. Amal Kabalan



Department Chairperson: Dr. Alan Cheville

Engineering Thesis Committee Member: Dr. Peter Mark Jansson

Engineering Thesis Committee Member: Dr. Alan Cheville

July, 2019

(Date: month and Year)

ACKNOWLEDGEMENT

I am greatly thankful to my advisor Dr. Amal Kabalan who has supported me these entire two years at Bucknell University. I would also like to thank my thesis committee advisors, Dr. Alan Cheville and Dr. Peter Mark Jansson for their valuable feedback and continuous support.

Bucknell University has been a place for me to experience diversity and meet lots of people from different culture. Moreover, it has also been a place where I have got the opportunity to meet many talented professors of different fields. Their insights and experiences about research have highly encouraged me to further continue my graduate studies. Being a teaching assistant in the ECE department, I have really enjoyed helping students with their course work.

I can't thank enough the international office for their support and guidance whenever I needed them. I would especially like to thank Bibiana Hernandez-Bello for her continuous support throughout two years of my graduate life. Moreover, Gretchen Fegley has been a very supportive person. I have never hesitated to seek any kind of help from her and she never failed to help me in any circumstance.

Special thanks to my husband who has supported me in any possible way that he could. It would not have been possible without him. I am very grateful to him. Also, my deepest gratitude to my family who has continuously supported me my entire life. My parent's encouragement has always been the strongest motivation for me to move forward in my career life.

TABLE OF CONTENTS

List of Tables	v
List of Figures	vi
Abstract	1
Chapter 1 Introduction	2
1.1 Renewable Energy	2
1.2 Global Energy Perspective	3
1.3 Discussion of Solar Energy	4
1.3.1 Evolution of Cost and Capacity: Photovoltaic Installations	6
1.3.2 Benefits and Limitations of Solar Energy	7
1.4 Outline of this Thesis	9
Chapter 2 Background	11
2.1 Fundamentals of the Solar Cell	11
2.1.1 Principle of Operation	11
2.1.2 Parameters of the Solar cell	13
2.2 Hierarchy of Different Generations of the Solar Cell	19
2.3 Micropillar Solar Cell	20
2.3.1 Planar (Conventional) Versus Micropillar Solar Cell	21
2.3.2 Radial and Axial p-n Junction Micropillar Solar Cell	23
2.4 ZnO/ZnTe Micropillar Solar Cell	23
2.4.1 Problem Statement	23
2.4.2 Motivation	24
Chapter 3 ZnO/ZnTe Solar Cell	30
3.1 Overview of Simulation Framework	30
3.1.1 Optical Simulation Solver	30
3.1.2 Electrical Simulation Solver	37
3.2 Properties of ZnO and ZnTe	41
3.2.1 Optical Properties	41
3.2.2 Electrical Properties	43
3.3 Structural Comparison of Device Models	44
3.3.1 Structural Details of Planar ZnO/ZnTe Solar Cell	45
3.3.2 Structural Details of ZnO/ZnTe Micropillar Solar Cell	47
3.4 Results and Discussion	53
3.4.1 Optical Analysis	53
3.4.2 Carrier (Electron-Hole Pairs) Generation Profile	55

3.4.3 Electrical Analysis	58
3.5 Summary	59
Chapter 4 Impact of Doping on ZnO/ZnTe Micropillar Solar Cell	61
4.1 Effect of Doping on Electrical Parameters	61
4.2 Effect of Auger Recombination	63
4.3 Optimized Doping Profile	66
4.4 Summary	67
Chapter 5 Performance Analysis of ZnO/ZnTe Micropillar Solar Cell	68
5.1 Effect of Pillar Length	68
5.1.1 Optical Analysis	68
5.1.2 Electrical Analysis	70
5.1.3 Summary	73
5.2 Effect of Pitch	74
5.2.1 Optical Analysis	74
5.2.2 Electrical Analysis	76
5.2.3 Summary	79
5.3 Effect of Pillar Diameter	79
5.3.1 Optical Analysis	80
5.3.2 Electrical Analysis	80
5.3.3 Summary	84
Chapter 6 Future Work and Conclusion	85
6.1 Possible Future Extensions	85
6.1.1 Analysis of ZnO/ZnTe Solar Cells with Triangular Surface Geometry	85
6.1.2 Analyzing the Effect of Radiative and Shockley-Read-Hall Recombination	86
6.1.3 Exploring the Effect of Different Metal Contacts	86
6.2 Conclusion	86
Chapter 7 References	88

LIST OF TABLES

3.1	Electrical Properties of ZnO	44
3.2	Electrical Properties of ZnTe	44
3.3	Performance Comparison for Different Structures of ZnO/ZnTe Solar Cell	60

LIST OF FIGURES

1.1	An illustration of the relative contributions of different sources of energy with respect to the total consumption in the world.	3
1.2	(a)Relative contributions of different sources of energy in meeting the energy demand of the USA. (b) Contributions from the sub-classes of renewables.	4
1.3	Best Research Cell Efficiency Chart of 2019 by National Renewable Energy Laboratory	5
1.4	New installed PV with global PV installed annually	6
1.5	Price history of stand-alone silicon photovoltaic solar cells showing ~250X reduction in price within ~35 years.	7
1.6	Illustration of Solar installation across the USA in 2018. The top 10 list for the US states with highest levels of installments is also shown on the left. California installed more solar capacity than any other states.	8
2.1	(a) Typical structure and workflow of a solar cell. (b) Band diagram of the p-n junction illustrating the carrier (electron/hole) flow.	12
2.2	Current -Voltage (I-V) characteristics of a solar cell in dark and illuminated condition. Different parameters of interest have been marked on the figure.	14
2.3	(a) 3D structure of a Micro/Nano-pillar solar cell. (b) Cross-section of one wire and the band-diagram of the radial p-n junction.	20
2.4	(a) Radial junction micropillar and (b) Axial junction micropillar structure.	22
2.5	(a) Band alignment among ZnO and ZnTe. (b) Carrier separation in ZnO/ZnTe type-II Core/Shell hetero-structure.	27
3.1	The steps for the optical simulation process of the Finite- Difference-Time-Domain (FDTD) solver.	32
3.2	Angle of incident light versus wavelength (μm) of the input source parameter for optical analysis	34
3.3	Time domain input signal from the plane wave source	35
3.4	Input spectrum of the source in frequency domain (spectrum versus wavelength (μm)). This is the Fourier Transfer of the input time signal.	36

3.5	Different steps for the electrical simulation process used in the DEVICE module.	39
3.6	Fitting of real and imaginary components (n, k) of the refractive index for ZnO with Material Explorer.	42
3.7	Fitting of real and imaginary components (n, k) of the refractive index for ZnTe with Material Explorer.	43
3.8	One electrical unit cell of a planar ZnO/ZnTe solar cell. Different layers of materials have been annotated on the figure.	46
3.9	Energy band-diagram for conventional ZnO/ZnTe solar cell. Bandgaps for ZnTe and ZnO are 2.24 and 3.3 eV, respectively.	46
3.10	One single pillar of (a) radial junction ZnO/ZnTe micropillar solar cell and (b) axial junction ZnO/ZnTe micropillar solar cell.	47
3.11	3-D Schematic of ZnO/ZnTe radial junction (core-shell) micropillar array solar cell.	48
3.12	Scenario of light absorption and charge transport in (a) planar ZnO/ZnTe solar cell (b) axial micropillar ZnO/ZnTe solar cell and (c) radial (core-shell) micropillar ZnO/ZnTe solar cell.	50
3.13	Energy band-diagram for a radial micropillar ZnO/ZnTe solar cell. Bandgaps for ZnTe and ZnO are 2.24 and 3.3 eV, respectively.	52
3.14	Comparison of (a) reflection (b) transmission and (c) absorption in three different solar cell structures (planar, radial micropillar and axial micropillar).	54
3.15	Carrier generation profile for planar ZnO/ZnTe solar cell. The respective layers have been marked in the figure.	56
3.16	Generation profile for axial junction ZnO/ZnTe micropillar solar cell, observed from (a) XZ plane (b) YZ plane and (c) XY plane at 2 nm depth. (d-f) Show similar generation profiles for radial junction ZnO/ZnTe micropillar solar cell, observed from (d) XZ plane (e) YZ plane and (f) XY plane at 3 nm depth.	57
3.17	(a) Current-voltage (I-V) and (b) Power-voltage (P-V) characteristics for different structures (planar and micropillar) of ZnO/ZnTe solar cell.	59
4.1	Effect of doping concentration on the (a) V_{OC} (b) J_{SC} (c) Fill factor and (d) efficiency of a radial micropillar ZnO/ZnTe solar cell.	62

4.2	Auger recombination profile for radial core-shell micropillar ZnO/ZnTe solar cell of 1.5 μm height.	64
4.3	Effect of different degree of Auger recombination and doping levels on the efficiency of radial micropillar ZnO/ZnTe solar cell.	65
4.4	Doping profile for radial core-shell micropillar ZnO/ZnTe solar cell of 1.5 μm height.	66
5.1	Effect of pillar-height on (a) transmission (b) reflection and (c) absorption percentage of a radial micropillar ZnO/ZnTe solar cell.	69
5.2	Effect of pillar-height on (a) V_{OC} (b) J_{SC} (c) fill factor and (d) efficiency of a radial micropillar ZnO/ZnTe solar cell.	71
5.3	Effect of pillar-height on (a) current density and (b) power density of a radial micropillar ZnO/ZnTe solar cell.	72
5.4	Effect of pitch of the pillars on (a) transmission (b) reflection and (c) absorption percentage of a radial micropillar ZnO/ZnTe solar cell.	75
5.5	Effect of pitch of the pillars on (a) V_{OC} (b) J_{SC} (c) fill factor and (d) efficiency of a radial micropillar ZnO/ZnTe solar cell.	77
5.6	Effect of pitch of the pillars on (a) current density and (b) power density of a radial micropillar ZnO/ZnTe solar cell.	78
5.7	Effect of diameter of pillars on (a) transmission (b) reflection and (c) absorption percentage of a radial micropillar ZnO/ZnTe solar cell.	81
5.8	Effect of diameter of the pillars on (a) V_{OC} (b) J_{SC} (c) fill factor and (d) efficiency of a radial micropillar ZnO/ZnTe solar cell.	82
5.9	Effect of diameter of the pillars on (a) current density and (b) power density of a radial micropillar ZnO/ZnTe solar cell.	83

ABSTRACT

The prime focus of the energy-research community in recent times has been replacing fossil fuels with renewable energy. Therefore, photovoltaic research areas are rapidly expanding in this era. The purpose of this work is to compare three different structural ZnO/ZnTe solar cell types (planar, axial micropillar and radial micropillar). The best optical and electrical performance has been obtained by the radial junction (core-shell) ZnO/ZnTe micropillar solar cell due to its pillar structure and radial junction. The unique advantage of the radial junction micropillar is that the angle of the incident light and the carrier collection is orthogonal. Therefore, the pillar can be long enough to absorb 90% of the incident light. We explored the effect of dimension of the pillar (height, pitch and diameter) on the optical and electrical performance of the ZnO/ZnTe core-shell micropillar structure. An exploration of height in the range between 1.5 μm to 4 μm was studied. The results demonstrated that increasing the pillar height increases both optical and electrical performance of the device. Pitch value between 0.2 μm ~ 0.6 μm was explored. Both the minimum pitch value (0.2 μm) and maximum pitch value (0.6 μm) presented the worst performance for the device. In addition, the shell thickness (ZnTe) between 70 nm ~ 130 nm was studied. A shell thickness of 70 nm showed promising results in terms of optical and electrical performance. The effect of doping concentration on the electrical performance and auger recombination rate of the core-shell ZnO/ZnTe solar cell has been studied in this work.

CHAPTER 1

INTRODUCTION

Energy is the backbone of the human civilization. With relentless growth of industrial activities and urbanization, the demand for energy is growing at a massive proportion. Since the beginning of the industrial revolution, fossil fuels (coal, natural gas and petroleum) have been the primary means to meet our energy demand. However, there are two major drawbacks of using these fossil fuels to harvest the energy. First, the reserve for such sources is limited and they will surely be depleted in the near future. Second and the most serious issue is their adverse effect on the environment. Combustion of the fossil fuel generates harmful greenhouse gas emissions [1] which contribute to the global warming and the climate change. Considering the criticality of both aspects, there has been a surge of interest in exploring the alternative sources of energy.

1.1 Renewable Energy

Renewable energy sources are the possible means to meet the energy demand of the civilization without disrupting the planet. Renewable energy is collected from sources which are naturally replenished on a human timescale [2]. The family of renewables primarily comprises solar energy, wind energy, tidal energy, geothermal energy, hydropower, and biofuels. These sources are yet to become comparable with fossil fuels in terms of contribution to the global energy demand. However, the process of steady switch-over to renewable sources is going on across the world at an accelerating pace.

1.2 Global Energy Perspective

Even though the fossil fuels are clearly known to be the primary contributors to the devastating climate change, they are still the major sources of energy. Figure 1.1 shows a pie-chart of the contributions from different sources towards the total global energy demand (data for 2015, source [3]). Collectively, fossil fuels (petroleum, coal and natural gas) provide 87% of the global energy supply. Nuclear energy contributes 4% and the renewable amount is only 9% of the total. Specifically, within the USA (Fig. 1.2 (a)), over 80% of the energy supplies come from fossil fuels. A mere 10% of the total energy demand is met through the use of renewable sources. The contribution from renewables can be further subdivided into several categories. Bio-fuels and hydro-electricity are the leading

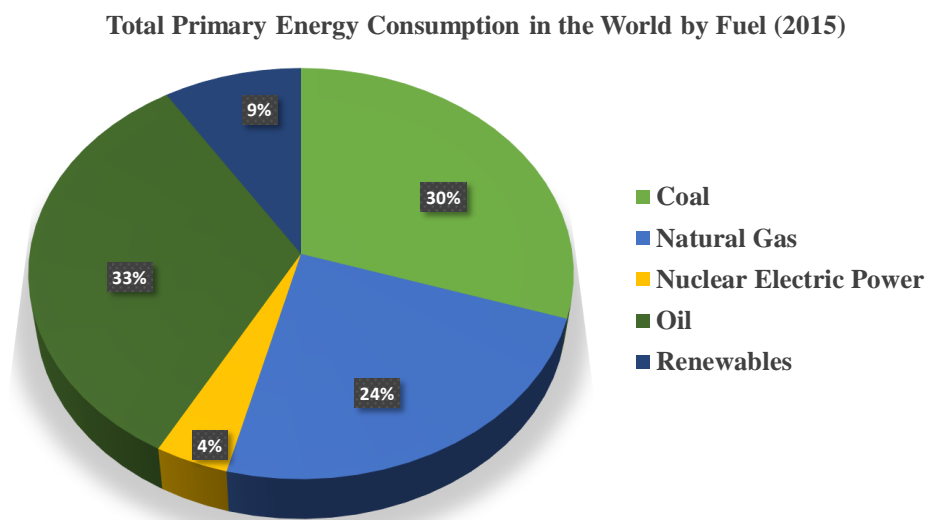


Figure 1.1: An illustration of the relative contributions of different sources of energy with respect to the total consumption in the world [3].

components in the renewable category. The solar energy only contributes 6% of the total renewable sources (Fig. 1.2 (b)). These data are for the year 2016 and are sourced from [4].

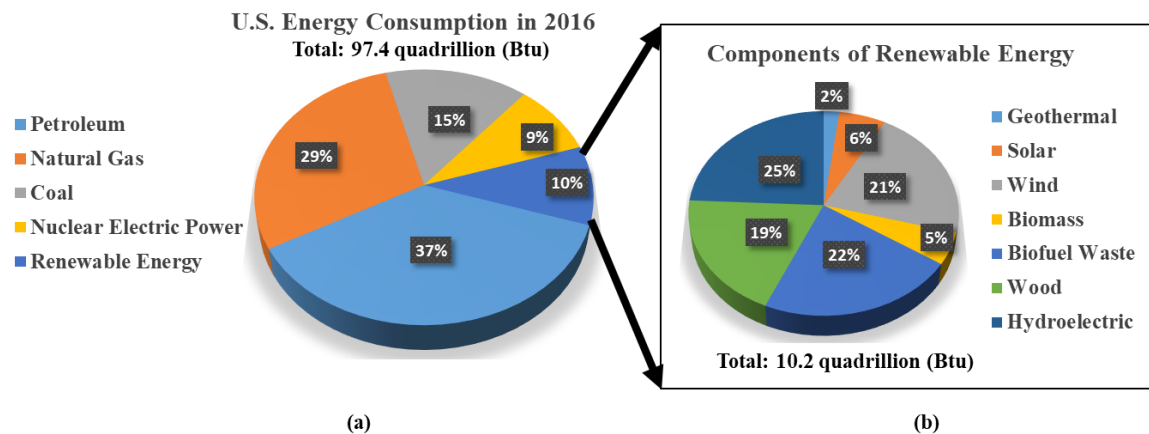


Figure 1.2: (a) Relative contributions of different sources of energy in meeting the energy demand of the USA. (b) Contributions from the sub-classes of renewables [4].

1.3 Discussion on Solar Energy

Among the different sub-classes of renewables, the solar energy is one of the most promising and sustainable options. The earth receives a tremendous amount of energy from the sun every day. This relentless source of energy can be harnessed to generate the electricity and thereby stored or used immediately. Even though the concept is simple, the implementation of devices and systems to perform the solar-to-electrical energy conversion is a challenge. Decades of work has been put into designing efficient devices to perform this conversion efficiently. Over time, the interest in this field has increased significantly and therefore monetary and intellectual investments have increased many fold.

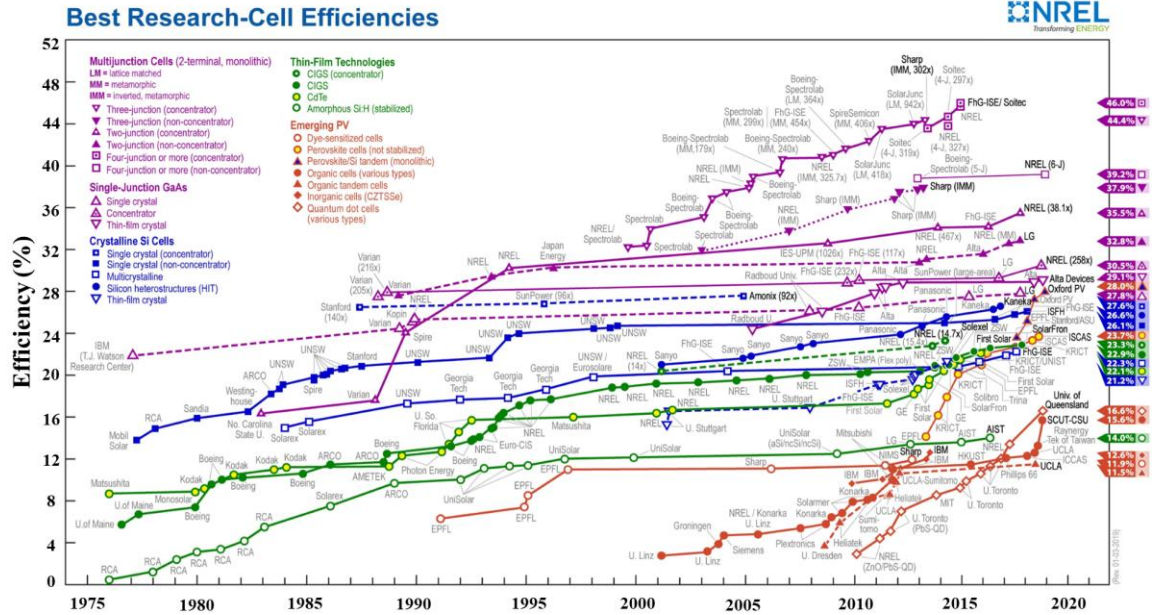


Figure 1.3: Best Research Cell Efficiency Chart of 2019 by National Renewable Energy Laboratory [5].

According to the National Renewable Energy Laboratory (NREL) record shown in Fig. 1.3, the crystalline silicon (non-concentrator) based solar cell has reached an efficiency of 26.1% and the multicrystalline silicon solar cell has reached to 22.3%. Using thin film technology, CdTe and CIGS-based solar cell ensured 22.1% and 22.9% efficiency respectively. On the other hand, the III-V compound semiconductor GaAs (single-junction, thin film crystal) promised 29.1% efficiency. Theoretically the multi-junction solar cell has a limiting efficiency of 86.6% (high concentration). Till now, the highest efficiency achieved by the multi-junction solar cell is 46.0% (concentrator). In addition, the emerging PV system is now the focus of much interest in the research community. Though the efficiency is still very low but the progress made over the years are significant.

1.3.1 Evolution of Cost and Capacity: Photovoltaic Installations

In line with the surging interest in renewables, the annually installed solar photovoltaic (PV) capacity in the world increased steadily from 1994 to 2018 [6]. Figure 1.4 illustrates that there has been a steady increase in solar PV capacity over the years globally. The plot

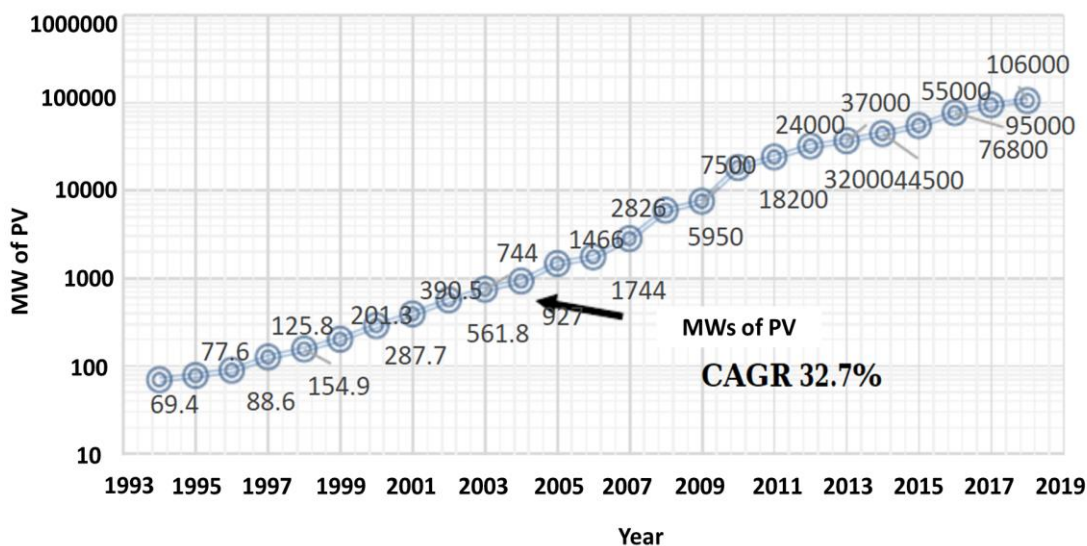


Figure 1.4: New installed PV with global PV installed annually [6].

has been presented in log scale. The numbers show that the compound annual growth rate (CAGR) is 32.7%. This has been a huge achievement for the solar community. Compared to the cost of ~\$6/Watt in 2010, the system price reduced to ~\$1.5/Watt in 2018. Figure 1.5 shows that the price of stand-alone silicon PV solar cells dropped from \$76/Watt in 1977 to \$0.3/Watt in 2015. This indicates an astonishing ~250X reduction in the price within a period of ~35 years [7].

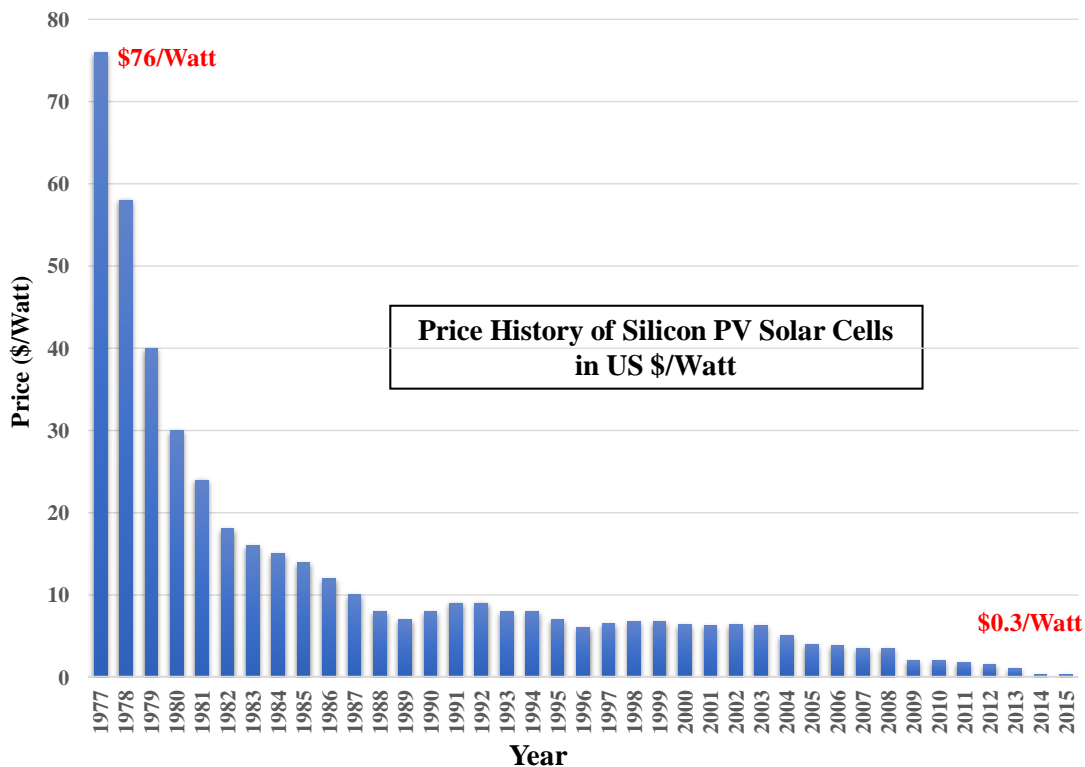


Figure 1.5: Price history of stand-alone silicon photovoltaic solar cells showing ~250X reduction in price within ~35 years [7].

On a different note, the state of California traditionally dominates the solar market in the USA. In 2018, the total installed capacity in California was 24,464 MW [8]. As shown in Fig. 1.5, markets in other states are also expanding and the top 10 list (Fig. 1.6) comprises the states of California, North Carolina, Arizona, Nevada, Texas, New Jersey, Massachusetts, Florida, Utah, and New York.

1.3.2 Benefits and Limitations of the Solar Energy

The solar energy is a truly renewable and self-replenishing source of the energy that can be harnessed in any geographic location on the earth. Use of solar energy has the potential

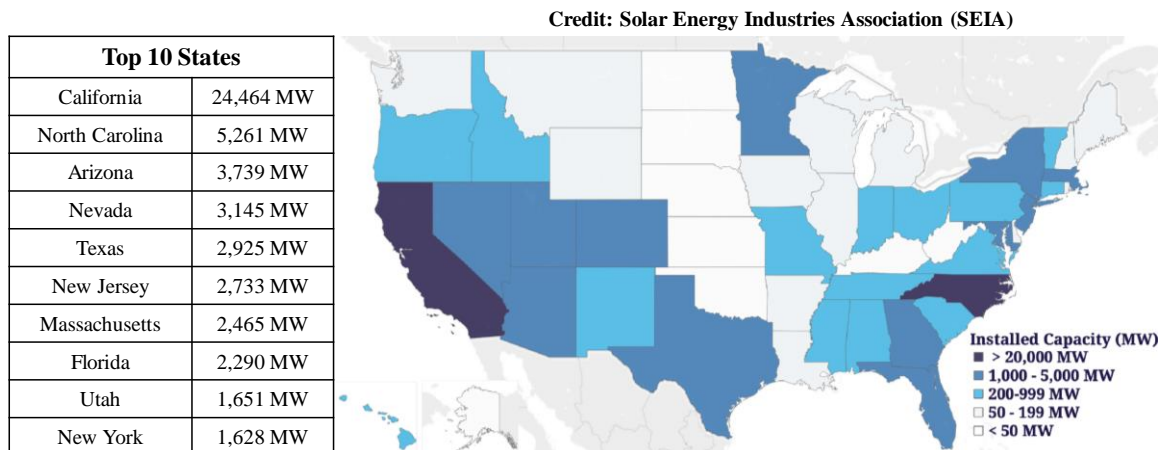


Figure 1.6: Illustration of PV installation across the USA in 2018. The top 10 list for the US states with highest levels of installments is also shown on the left. California installed more solar capacity than any other states [8].

to provide many benefits over the conventional fossil fuels [9]. The solar energy has the capability to achieve the following benefits:

- Generate energy without greenhouse gas emission
- Diversify energy supply and ensure sustainable growth
- Create new jobs in installation, operation and maintenance
- Stabilize energy prices
- Ensure reliable and resilient supply using distributed and modular production
- Improve public health environmental conditions by effectively lowering pollution
- Ensure an inexhaustible supply of the energy.

With all of these outstanding benefits, there still exist few limitations. The major limitations of the solar energy are enlisted below.

- Cost of production in most applications is still high compared to that of conventional fossil fuel sources
- The energy output is dependent on weather conditions
- Expensive storage systems would be required to ensure the energy reserve during night time
- Sunlight capture requires a lot of space.

These limitations are not show-stoppers for the solar energy research as the benefits far out-weigh the drawbacks. As a result, exploration of efficient and optimized solar cells has continued to be a field of strong research interest in the scientific and industrial communities.

1.4 Outline of this Thesis

The prime purpose of this thesis is to contribute to the ongoing scientific efforts to improve and investigate the solar cell structures. This work focuses on the performance analysis (optical and electrical) of the ZnO/ZnTe core-shell micropillar array solar cell. The next chapter will provide a brief background on the basic concepts of the solar cell operation, performance parameters and different types. It will also discuss the basics of the micropillar solar cell and provide motivation for the use of ZnO/ZnTe material system. Chapter 3 will discuss the simulation framework and input parameters used for this work along with the optical and electrical properties of ZnO and ZnTe. It will also present a comparison of different device models (planar, radial and axial) for the ZnO/ZnTe solar cells. The fourth chapter will discuss the impact of various doping profile on the ZnO/ZnTe micropillar solar

cell. The effect of doping levels and degree of recombination will be analyzed. Chapter 5 will discuss the results of the performance analysis of the radial ZnO/ZnTe micropillar solar cell, where the effect of pillar length, pitch, and pillar diameter will be analyzed. Finally, chapter 6 will provide a future outlook and summarize this work.

CHAPTER 2

BACKGROUND

This chapter focuses on the basic description of the operating principle and associated performance metrics of the solar cell. A short review of the evolution of different generations of solar cells will also be presented here.

2.1 Fundamentals of the Solar Cell

The solar cell is a device that converts energy from the photons of light to usable electrical energy. It operates using the fundamental principles of carrier generation and transport in a semiconductor. Careful co-design and optimization is required to fabricate an efficient solar cell.

2.1.1 Principle of Operation

The basic component of a solar cell is a p-n junction. A p-n junction is formed by joining p-type and n-type semiconductor materials. Excess electrons from the n-type try to diffuse towards the p-type and vice versa. The movement of electrons and holes results in an electric field at the junction which is called the depletion region. This region possesses an electric field which results due to the separation of the migrating minority carriers from either side of the p-n junction. This electric field in the depletion region is a key component in solar cell design.

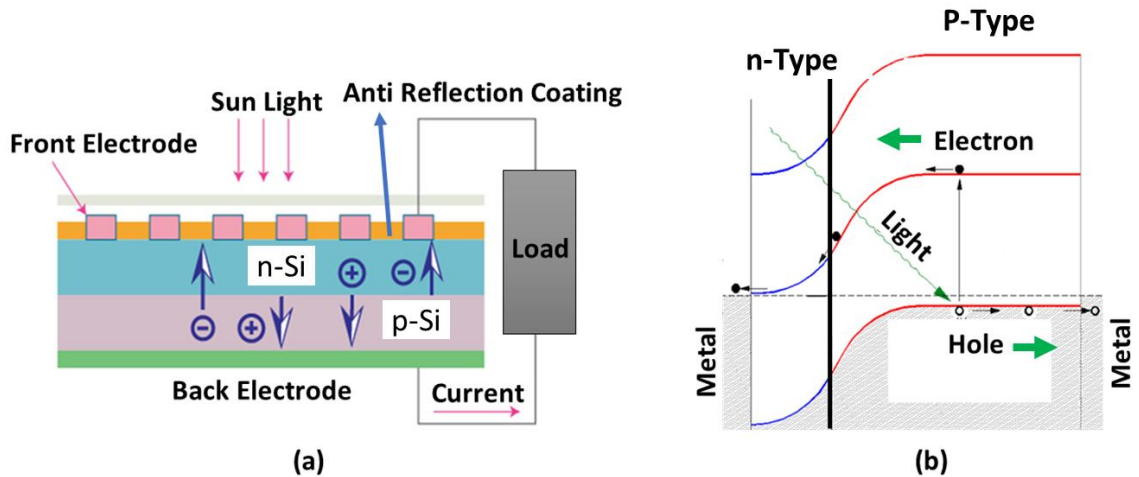


Figure 2.1: (a) Typical structure and workflow of a solar cell. [10] (b) Band diagram of the p-n junction illustrating the carrier (electron/hole) flow [11].

Fig. 2.1(a) shows the simplified structure of a typical Si solar cell. The top layer is n-type silicon and the bottom layer is p-type silicon in the device structure. Anti-reflection coating is used on the surface of the n-type silicon layer (top layer) to minimize the reflection of sunlight. This is a type of optical coating which is applied at the surface of the solar device to reduce the loss of light and enhance the efficiency of the cell. Electrodes are placed at the top (front electrode) and bottom side (back electrode) to collect the generated holes and electrons inside the device layers. To be specific, the top layer is called the emitter layer and the bottom layer is known as the base layer. If the incident photon has energy greater than that of the silicon band gap (1.1 eV), an electron-hole pair will be generated. If the generated electron-hole pair recombines before it reaches the p-n junction, the carriers are lost, and no electrical current/power can be generated. For this reason, preventing recombination is one of the major goals of cell design.

Figure 2.1(b) shows the transport mechanism of electrons and holes in the silicon solar cell. An electron absorbing the photon energy gets excited and goes to the conduction band from the valence band. If the photo-induced minority carriers reach the depletion region, they are swept across the junction by the electric field. The minority carrier electrons at the p layer drift toward the n-type layer due to the electric field and become majority carriers. Similarly, the minority carrier holes at the n-type layer drift toward the p-type layer and become majority carriers. Minority carriers cannot pass through a semiconductor-metal boundary. Thus, recombination is prevented. This mechanism allows collection of the photo-generated carriers thereby creating an electric current across the external terminals of the solar cell. An important aspect to keep in mind is the minority carrier lifetime. This is the average time between recombination events of minority carriers. Note that the minority carrier lifetime largely depends on the doping concentration of the material [12]. The acceptor and the donor concentration must be as large as possible to achieve high efficiency solar cells [13].

2.1.2 Parameters of the Solar cell

This section provides a brief description of different characteristic parameters of a solar cell. These parameters are associated with the operation of the cell and are discussed in association with their I - V characteristics. The parameters that are described in this section will be used for the performance assessment for both planar and micropillar type solar cells. The optimization efforts for a solar cell are effectively driven by the goal of improving these performance parameters.

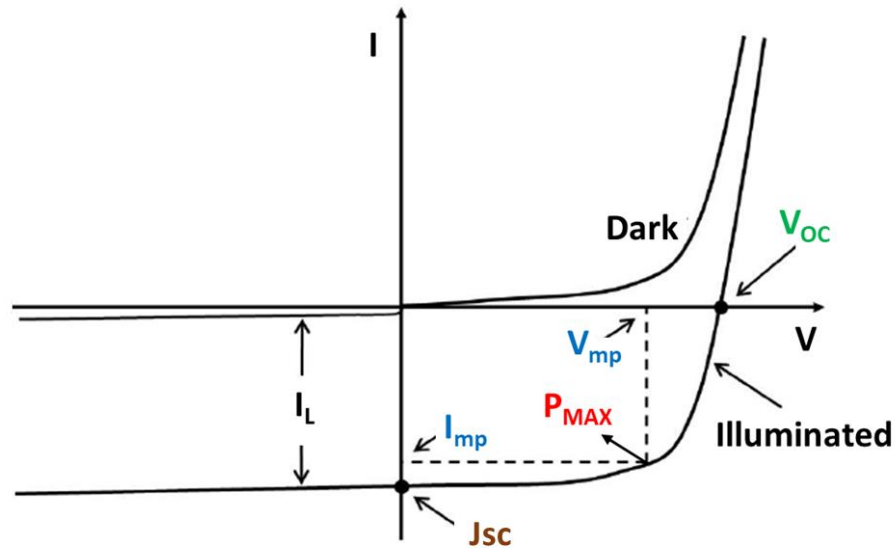


Figure 2.2: Current -Voltage (I - V) characteristics of a solar cell in dark and illuminated condition [14]. Different parameters of interest have been marked on the figure.

- **Open Circuit Voltage (V_{OC})**

The maximum voltage that can be obtained across the terminals of a solar cell is called open circuit voltage (V_{OC}). This parameter can be obtained from the I - V characteristics of a solar cell in both dark and illuminated conditions (Fig. 2.2, [14]). In darkness, the solar cell behaves just as a regular p-n junction. However, when illuminated, photo-generated carriers give rise to the additional current in the opposite direction of the typical current flow in a forward biased diode. Hence, the photo-generated current actually represents a reverse bias current in the p-n junction. With sufficiently high forward bias, the forward current flow cancels out the photo generated reverse current and the overall current will be zero. The voltage that corresponds to the zero total current actually represents the open

circuit voltage of a solar cell. Open circuit voltage (V_{oc}) is related to the carrier concentration and can be determined using the following relation:

$$V_{oc} = \frac{KT}{q} \ln \left[\frac{(N_a + \Delta n)\Delta n}{n_i^2} \right] \quad (2.1)$$

$$\frac{kT}{q} = \text{thermal voltage}$$

N_a = doping concentration

Δn = excess carrier concentration and

n_i = intrinsic carrier concentration

- **Short Circuit Current Density (J_{sc})**

The short circuit current density (J_{sc}) represents the maximum amount of current density (current per unit area) that can be obtained from a solar cell under illumination when the voltage across the solar cell is zero (Fig. 2.2). Mathematically, the short circuit current of a solar cell is given by

$$J_{sc} = -I_{ph} \quad (2.2)$$

Where, I_{ph} is the photo-generated current which is given by,

$$I_{ph} = qAG(L_h + L_e) \quad (2.3)$$

Where,

q = Charge of the photo-generated carrier

A = Effective area of solar cell

G = Generation rate

L_h = Diffusion length of hole

L_e = Diffusion length of electron

From equations (2.2) and (2.3),

$$J_{SC} = -qAG(L_h + L_e) \quad (2.4)$$

Note, the open circuit voltage (V_{OC}) and the short circuit current (J_{SC}) differ with the change of the minority carrier lifetime [15].

- **Fill Factor (FF)**

The Fill Factor (FF) is essentially a measure of quality of the solar cell. It is the ratio of the voltage multiplied with the current at the maximum power (P_{MAX}) point (Fig. 2.2) to the multiplication of open circuit voltage and short circuit current. P_{MAX} can be interpreted graphically (Fig. 2.2). Fill factor is given by

$$\text{Fill Factor} = \frac{V_{mp} I_{mp}}{V_{oc} J_{sc}} \times 100\% \quad (2.5)$$

Where, V_{mp} = Voltage at the maximum power point,

I_{mp} = Current at the maximum power point,

V_{oc} = Open circuit voltage

J_{sc} = Short circuit current.

The maximum theoretical value of the fill factor of a solar cell is unity. Hence, while optimizing/designing a solar cell, it is important to ensure a fill factor that is as high as practical.

- **Efficiency (η)**

The efficiency of a solar cell is defined as the ratio of power at the maximum power point (V_{mp} , I_{mp}) to the input power of solar irradiance. Mathematically, the efficiency of a solar is given by

$$\text{Efficiency} = \frac{P_{mp}}{P_{in}} \times 100\% \quad (2.6)$$

Where, power at maximum point (P_{mp}) is given by,

$$P_{mp} = V_{mp} \times I_{mp} = FF \times V_{OC} \times J_{SC} \quad (2.7)$$

Here,

P_{in} = Input power of the solar irradiance

FF = Fill Factor

Therefore, the efficiency of the solar cell is given by

$$\eta = \frac{FF \times V_{OC} \times J_{SC}}{P_{in}} \times 100\% \quad (2.8)$$

It is evident from equation (2.8) that the efficiency of a solar cell increases with the increase of the open circuit voltage, short circuit current, and fill factor of the solar cell.

2.2 Hierarchy of Different Generations of Solar Cells

The design and development of the solar cell technology has taken decades of the academic and industrial research to evolve into a mature industry. Based on the timeline and principles of design and new material systems, solar cells can be categorized in three generations as described below.

- First Generation (1G) PV Materials:

These are made of silicon (Si) including polysilicon and monocrystalline silicon. These types of solar cells have achieved 26.1% efficiency for the single crystal (non-concentrated) silicon and 22.3 % for the multicrystalline silicon [5]. Because of their relatively high efficiency, these cells continue to dominate the commercial market in spite of their high production cost.

- Second Generation (2G) PV Materials:

The second generation (2G) solar cell has been developed with the aim to reduce the production cost over the first generation (1G). Second generation solar cells consist of thin films such as amorphous silicon (a-Si) solar cell, cadmium telluride (CdTe), and copper indium gallium diselenide (CIGS). With the advent of thin film technology in 2G solar cells, the bulk material in the 1G solar cell is replaced with the thin film. As a result, the material cost is reduced. However, the efficiency is 23.4 % for CIGS, 22.1% for CdTe, and 14% for amorphous silicon (a-Si) solar cell, which is less than the efficiency of the 1G

solar cell [5]. The key factor that is favorable in 2G is the reduction in the amount of material needed and low cost per delivery, but the demand for the larger surface area to compensate for the low efficiency is an issue. Note that, the CdTe is made up of cadmium and tellurium mixed with the zinc cubic crystal structure. CdTe is cheaper than silicon but not as efficient as silicon material [16]. Although CdTe is cheaper, it is toxic for the environment.

- *Third Generation (3G) Solar Cell*

Main types of solar cells within the third generation are dye-sensitized cells, perovskite cells, organic cells, organic tandem cells, inorganic cells and quantum dot cells [5]. In this generation, significant attention has been paid to optimize the charge collection in the solar cell. Organic materials have low cost and high absorption capability. Nanocrystal solar cells, photoelectrochemical (PEC) cells, grätzel cells, dye-sensitized hybrid solar cells, and polymer solar cells are part of the 3G family [16]. The design of these types of solar cells are at the nanoscale and micro scale. Third generation also includes multi-junction solar cells, which currently hold the lead on performance (>47 % efficiency). Another new development, the perovskite solar cell, has obtained efficiency of 24-28% on a very small area [5]. All these types of solar cells in the 3G technology are available and inexpensive. Although third-generation solar cells have limited stability and performance compared to that of first- and second-generation solar cells, they have already been commercialized and research interest for their improvement is increasing [17].

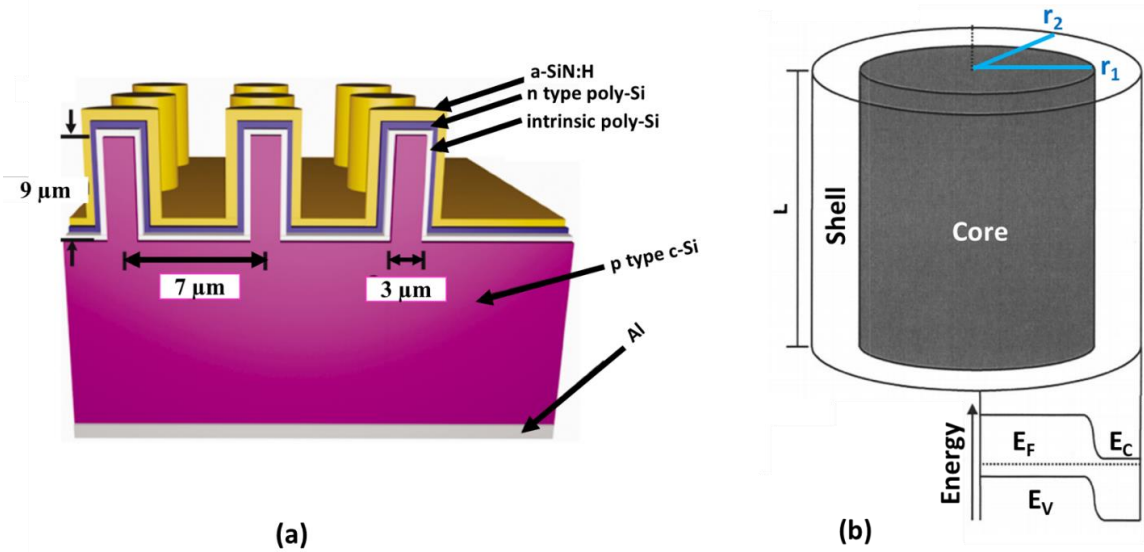


Figure 2.3: (a) 3D structure of a micropillar solar cell. [18] (b) Cross-section of one wire and the band-diagram of the radial p-n junction [19].

2.3 The Micropillar Solar Cell

While the mechanism and structure described in Fig. 2.1 is a general guideline for solar cell design, several variants have been proposed in the literature. Conventionally, the p-n junction of the solar cell is designed with layers of parallel planes. There can be several layers (e.g. anti-reflecting coating, front electrode, back electrode) of materials in addition to the p and n semiconductor layers. However, all of these layers are parallel to each other and distributed vertically in the same geometric plane. While this conventional planar structure has come to maturity and been commercialized, new structures of solar cells are also being actively sought after. The micropillar solar cell structure is one of the most promising versions being actively explored. The silicon-based technology has served its purpose successfully for decades and attained maturity.

2.3.1 Planar (Conventional) Versus Micropillar Solar Cell

A micropillar solar cell is constructed by changing the planar geometry of the solar cell to a cylindrical geometry. Fig. 2.3 (a) shows the 3D structure of a micropillar solar cell. The exterior layer of the nanorod is usually known as the ‘shell’. The interior layer of the nanorod is called the ‘core’. The exterior emitter layer (‘shell’) is of n-type and the interior absorber layer (‘core’) is of p-type. Such p-type and n-type layers form a radial p-n junction. Fig. 2.3 (b) depicts the internal structure of a single nanorod and the band diagram of the radial p-n junction. Light is incident on top of the nanorods in the cell (practically at small angles). However, carriers are mainly generated at the absorber (‘core’) layer. These photo-generated carriers are collected by the radial p-n junction. Note, the length of the nanowires is in the direction of the incident light whereas the extraction of carriers is in the orthogonal direction with the incident light (provided that the minority carrier diffusion is very insignificant in parallel with the incident light [19]). The comparison between planar and micropillar solar cells is as follows:

- The absorption efficiency is quite limited in planar solar cells [20]. Micropillars located at the surface of the solar cell exhibit higher degree of absorption of the incident light. This surface structure improves the light harvesting capability of the solar cell by creating multiple interactions of the incident light within the gaps between the pillars. The micropillar structure increases the surface-to-volume ratio [21]. As a result, the maximum amount of the incident light gets trapped.

- The recombination of the generated electron-hole pairs in an ordinary solar cell is a major concern [22]. Less expensive materials usually exhibit high levels of impurities and defect states, leading to a short minority carrier-diffusion length [23]. Therefore, using these materials in a planar solar cell drastically limits the carrier collection and reduces the efficiency. On the other hand, the radial structure of p-n junction allows carrier collection even with shorter minority carrier diffusion length and therefore permits use of less expensive materials [24]. Thus, micropillar solar cells radically solve the issue with the collection of generated carriers.
- The 3-D wire geometry of the micropillar solar cell reduces reflection of incident light over that incurred by cells with planar structure. Hence, the absorption efficiency further improves [25].
- Upgraded band tuning capabilities have been reported [26] for micropillar solar cells, which creates an additional knob for the performance tuning and design.

In summary, a micropillar structure can provide a good number of unique advantages over the planar solar cells. Therefore, the micropillar structure has been garnering immense interest in the academic community for years.

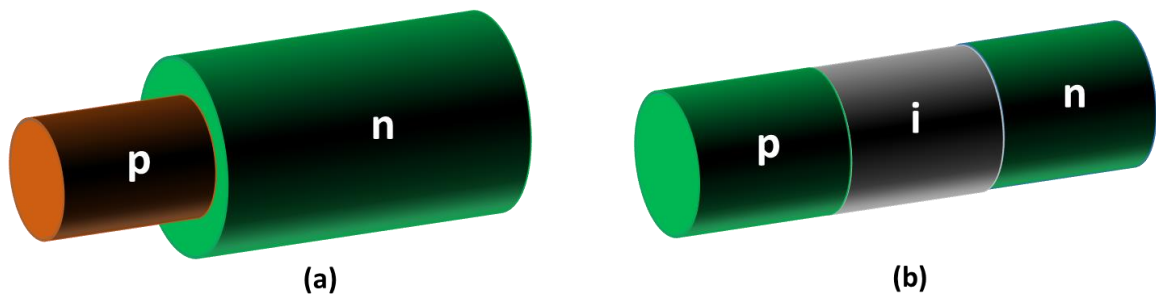


Figure 2.4: (a) Radial junction micropillar and (b) Axial junction micropillar structure.

2.3.2 Radial and Axial p-n Junction Micropillar Solar Cells

Two major variants of micropillar solar cells have been reported in the literature. The first kind is the radial micropillar cell as shown in Fig. 2.4 (a). In this version, the p-n junction is formed radially across the cylindrical pillar. The other type is called the axial micropillar solar cell (Fig. 2.4 (b)). In this version, the p-n junction is formed across the axis of the cylindrical pillar. Both of these structures have their own benefits and limitations. The process of fabrication is also very different for these structures. Both of these two variants of micropillar solar cells have benefits over the planar solar cell structure. As part of this work, both of these versions of solar cell will be explored and their respective performance metrics will be compared against each other.

2.4 ZnO/ZnTe Micropillar Solar Cell

Different material systems have been reported to form micropillar structures. The ZnO/ZnTe pairing is one of the most promising combinations of materials especially for micropillar solar cells. This work is focused on ZnO/ZnTe-based micropillar solar cells. The motivation for this particular version of the solar cell is discussed in Section 2.4.2.

2.4.1 Problem Statement

Si, being the primary material for photovoltaic as well as other semiconductor industries (e.g. computer chip design, analog electronics, digital memory), has very high demand across the world. Conventional first-generation crystalline Si has allowed photovoltaics to

achieve 26 % efficiency [5]. Almost 40-50% of the cost of a finished silicon-based module comes from the input system needed to fabricate highly purified silicon [27]. However, c-Si has reached higher efficiency but it is not cost-effective. Hence, new material systems are being introduced along with novel structures. Even after numerous innovations, high efficiency and cost minimization are still a challenge for solar cells. Compound semiconductors formed from II-VI material (II=Zn, Cd, Hg and VI=O, S, Se, Te) are key materials which are promising enough to compete with the Si solar-cell industry [34].

The target of our research is to model, analyze, and optimize novel solar cell structures based on II-VI semiconductor materials. One such material, CdTe has already been extensively developed. The thin-film CdTe have already been commercialized and have achieved 22.1 % efficiency [5]. However, the fact remains that cadmium is toxic, and production of these thin films are damaging to the environment [27]. We chose instead to focus on another II-VI material, ZnTe, which has not been extensively investigated and which does not present danger to the environment. The motivation for choosing II-VI materials (and specially ZnO/ZnTe) for our research is discussed below.

2.4.2 Motivation

Semiconductor materials of the II-VI group have become highly demanding in the PV research because of their decent optical and electrical properties. These materials exhibit high photosensitivity, direct optical transition, and high absorption coefficient. Undoubtedly the main goal for the photovoltaic research is to attain a highly efficient solar

cell with lower consumption of the material by making the cell thinner. Thinner cells will not only lower the usage of the material but also decrease the production cost and time. II-VI semiconductor materials seem to meet all these challenges. Among all II-VI materials, ZnO is unique in having high electron mobility, wide and direct bandgap, and good thermal conductivity. All these properties make ZnO suitable for photovoltaic applications [28]. However, ZnO by itself suffers from some limitations in solar cell applications. It is very difficult to make p-type ZnO as it is naturally n-type [29]. Therefore, forming a p-n junction using only ZnO is a challenge. However, there have been demonstration of the ZnO-based homojunction solar cell [30]. The issue is that, due to the high band-gap of ZnO, the homojunction solar cell mainly absorbs UV light (very little visible light) [31]. In addition to that, the theoretical efficiency limit of bulk ZnO is limited to only 7% efficiency [27].

One interesting idea to reduce the high bandgap of ZnO (3.3 eV), is to stack some other materials such as ZnS or ZnTe in order to reduce the bandgap of the compound material overall [27]. II-VI material, ZnTe, can be combined in heterojunction structure with ZnO to overcome these limitations [32]. ZnTe material naturally has a p-type behavior because its defects (such as zinc vacancy) lie within the valence band rather than within the bandgap. Hence ZnTe can be easily integrated with ZnO to form a p-n junction. In addition, strong photo-response has been observed in the range of 2.3eV to 3.6 eV in n-ZnO/p-ZnTe solar cells [33]. The solar cell structure based on the combination of these two materials has the following advantages:

- It has been shown that n-type ZnO has low resistivity and also has chemical compatibility with ZnTe [28]. Moreover, ZnTe has a lower bandgap (2.23-2.29 eV) compared to ZnO (3.3 eV) [33]. As a result, the combination, ZnO/ZnTe exhibits a lower effective bandgap and therefore can absorb energy in the visible light spectrum [34].
- ZnO/ZnTe heterojunction provides another major advantage if used in a core/shell configuration. ZnO/ZnTe yields a type II core/shell structure where the conduction and valence bands of ZnTe are at a higher energy level than those of ZnO (Fig. 2.5(b)). Hence, an inherent special separation of the electrons and holes is possible in this material system [35]. That leads to significant improvement in carrier lifetime and promises greater efficiency in the solar energy conversion.
- ZnO is usually n-type and ZnTe is normally p-type; therefore, n-ZnO/p-ZnTe can easily be fabricated.
- ZnO and ZnTe are nontoxic and environmentally friendly [36]. Both of these materials are good replacements for heavy-metal-based materials
- A ZnO/ZnTe solar cell has an effective bandgap of 1.17eV where the optimal bandgap of a solar cell is 1.45eV [37]. In addition, the band alignment between these two materials can be modified using different growth methods [38]. Fig. 2.5(a) shows the band alignment between ZnO and ZnTe. The band gaps of ZnO and ZnTe are shifted from 3.361/2.337 eV for unstrained ZnO/ZnTe (dashed lines) to 2.615/1.364 eV for the strained bulk materials (solid lines).

- ZnO/ZnTe structure is also very promising in realizing the micropillar type solar cell. The geometric structure of the micropillar solar cell increases the surface area [39], as discussed before. But, the materials which have high surface recombination velocity will not be good choices to obtain an optimal design micropillar solar cell. ZnTe has low surface recombination velocity [40] and hence using this material as the surface layer will improve efficiency of a micropillar solar cell.
- According to Shockley–Quiesser model, ZnO/ZnTe quantum well heterostructures could reach 30% efficiency, while planar ZnO/ZnS can only achieve 19% efficiency, and core-shell quantum well structures of ZnO/ZnS only 23% [27].

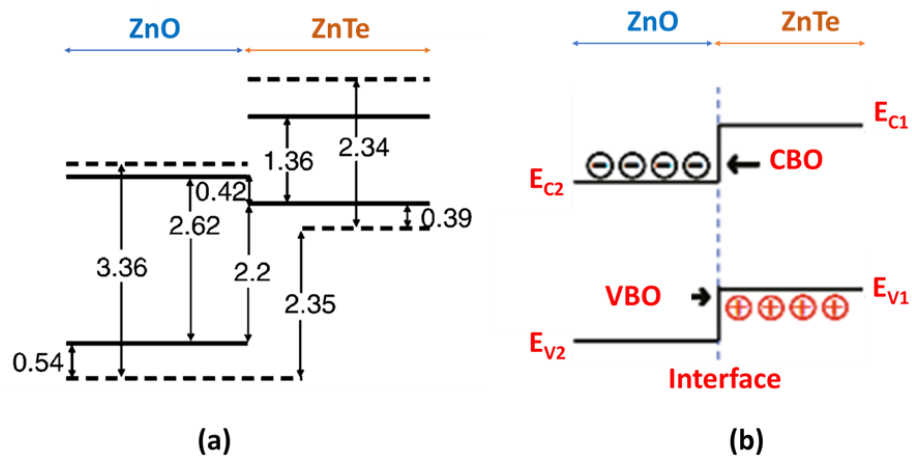


Figure 2.5: (a) Band alignment among ZnO and ZnTe [27]. (b) Carrier separation in ZnO/ZnTe type-II Core/Shell hetero-structure [27].

The distinct advantages of the ZnO/ZnTe solar cell motivated our focus in this research work. We know that the limiting efficiency of a single-junction solar cell is 33.1% [41]. Si – based (indirect bandgap, 1.1 eV) solar cells have achieved 26.1% efficiency [5]. Slightly better efficiency is promised by the single-junction III-V compound GaAs (direct bandgap,

1.4 eV) cells. These cells, with their higher electron mobility when compared with silicon [42], hold the highest efficiency record of 29.1% among typical cells shown in Fig. 1.3. However, As is toxic for the environment. The current configuration with highest efficiency of 22.1 % efficiency is another II-VI group material, CdTe [5]. But, they are toxic as well.

Silicon, being a very poor absorber, requires a thick layer (150 μm – 200 μm) to absorb most of the light. Whereas GaAs, having high absorptivity, requires only a few micrometers of thickness which makes it lightweight and flexible [43]. Also GaAs is resistant to UV and moisture, so used in space applications. However, its high cost prohibits its use commercially [44]. In addition, unlike silicon, gallium is rare and arsenic is environmentally toxic [45]. Even though Si is abundant in the environment [46], the silicon-based cell is not easy to transport because of its rigidity and heavy weight [47].

Multi-junction solar cells have a much higher limiting efficiency of 86.8% under highly concentrated sunlight [48]. To date, the highest efficiency of 46.0% has been achieved using III-V semiconductor material with a maximum of four junctions shown in Fig 1.3. However, the fabrication process is difficult and complex for multi-junction solar cells.

The II-VI compound CdTe-based solar cell reached almost 22.1 % efficiency with absorber layer thickness of only 5-10 μm to absorb maximum light because of its high absorption coefficient [49]. Moreover, CdTe-based solar cells are already commercialized in the market and a huge segment of thin film technology relies on CdTe materials. In terms of cost, CdTe photovoltaics are currently generating electricity mostly equal to the cost of the

fossil – fuel energy sources [50]. This is a huge improvement in the photovoltaic sector. However, the toxicity issue of cadmium is still a concern. Though CdTe has its huge advantages in the solar community, but replacing CdTe with another II-VI material, ZnTe, will make the environment safe. We see ZnTe as a viable alternative to the current choice, CdTe.

CHAPTER 3

THE ZnO/ZnTe SOLAR CELL

This chapter will present a simulation-based study of the ZnO/ZnTe solar cell. First, a detailed description of the simulation framework will be discussed. The physics-based principles of the simulation will be discussed along with the solution mechanism. Next, simulated properties of the ZnO/ZnTe solar cell will be discussed.

3.1 Overview of Simulation Framework

To model a solar cell, it is necessary to perform both optical and electrical simulations. In this work, the Lumerical Finite Difference Time Domain (FDTD) solver (Release: 2019a r5, Version: 8.21.1906) has been utilized for optical simulations. The Lumerical DEVICE simulator (Release: 2019a r5, Version: 7.3.1906) has been used for analyzing the electrical performance of the device.

3.1.1 Optical Simulation Solver

The optical properties of a device determine how the device interacts with the incident light. There are numerous methods available for the simulation of optical performance of a device. As mentioned in Section 3.1, our research work utilizes the Finite-Difference-Time-Domain (FDTD) technique. FDTD is one of the most popular methods used in the solution of electromagnetic wave propagation problems in the time domain. Maxwell's equations [51] determine the electric and magnetic behavior of any device that interacts

with electromagnetic waves. These equations can be solved either in the time domain or in the frequency domain. The FDTD method uses the partial differential equation (PDE) terms of the Maxwell equations [52]. While solving the Maxwell equations using the FDTD method, electric (E) and magnetic (H) fields are considered discrete in both space and time.

The FDTD method can be based on the 2D or 3D Maxwell solver. The FDTD solver is extensively used for its very simple application. K. Yee first introduced this method [53] and several improvements have been made over the years. It has been significantly applied in the optical and photonic devices sector. Moreover, FDTD is being widely used for simulations in plasmonics [54], solar cells, metamaterials [55] and integrated optics [56] among other applications. This method generally calculates the direction of electromagnetic fields on a rectangular finite difference grid. Eventually it can handle complex arbitrary geometries and non-linear materials. Most importantly, this method does not consider any approximations or assumptions and provides the maximum accuracy of the solutions [57]. The finite mesh size and finite sized time step are the only variables that are assumed by the FDTD solutions. The most important advantage of the FDTD solution is that it provides broadband results with only a single simulation. FDTD is particularly useful in analyzing devices whose feature sizes are on the order of a wavelength or smaller. However, the difficulties that have been identified so far to solve the Maxwell's equations with finite difference time domain solutions are material interfaces [58]. Moreover, a large number of time steps is required for the simulation process and a medium with high permittivity needs a fine grid [58].

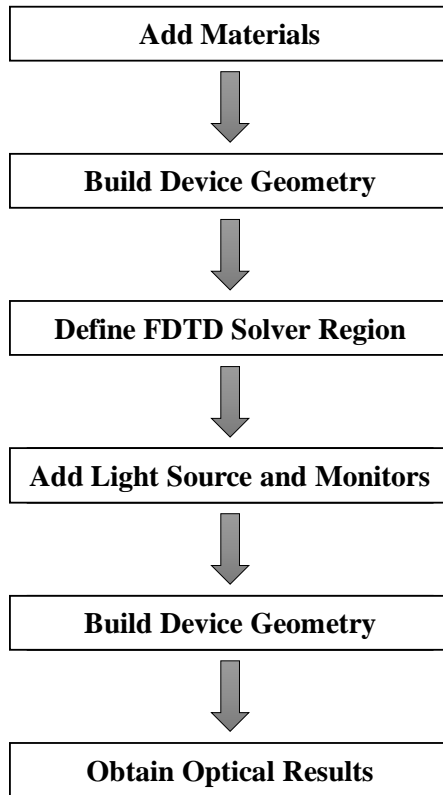


Figure 3.1: The steps for the optical simulation process of the Finite- Difference-Time-Domain (FDTD) solver.

A flow-chart for the steps of the optical simulation process is shown in Fig. 3.1. While setting up a simulation file, the first step is to add materials required for the project in the project file (*filename.fsp*). To add the materials in the project file, optical properties of the materials are defined according to their models. In order to build the entire structure of the device, structures from the *structure* menu (such as rectangular, cylindrical and triangular objects) are added in the file. Even more complex geometries can be built by using the *Lumerical Scripting Language* [59]. The FDTD solver region determines the simulation area or volume that can be either 2-dimensional or 3-dimensional. Any structures, sources

or monitors that are not within the simulation region (unit-cell) do not take part in the simulation process. Simulation time, boundary conditions, and mesh settings are defined by the solver region as well. In fact, while working with a solar cell, the periodic nature of this device can be employed using periodic boundary conditions to minimize memory area and simulation time. The periodic boundary condition allows the solver to calculate the response of the entire device system by simulating only a unit cell. Periodic conditions can be applied only when the entire system is periodic both in physical structures and electromagnetic fields. Different sources (*e.g.* point sources, gaussian and cauchy/lorentzian beam sources, plane wave sources, total-field scattered-field sources, mode sources) are available in the FDTD solver. Sources are added to inject electromagnetic fields within the simulation region to carry out the optical simulation analysis. This injected light propagates and interacts with the structure within the simulation region.

For the entire research work of this thesis, a plane wave source has been employed in all of the project files. However, plane wave sources are of three different types: BFAST, diffracting and periodic/bloch [60]. The diffracting plane wave source is used when a PML (Perfectly Matched Layer) layer is used in all directions (x , y and z). In addition, BFAST (Broadband Fixed Angle Source Technique) is used when the periodic structure is illuminated with a broadband source at an angle. This technique will allow the users to get the broadband simulation results at an angled illumination. Hence, monitors are applied to record the simulation results. The types of monitors that are available in this FDTD solver are index monitor, time monitor, frequency domain power and profile monitor [60].

Whereas index monitors and time monitors can only measure the refractive index of the structure and the electric fields over time, a frequency-domain power monitor provides transmission, reflection, and spatial-field profiles as well.

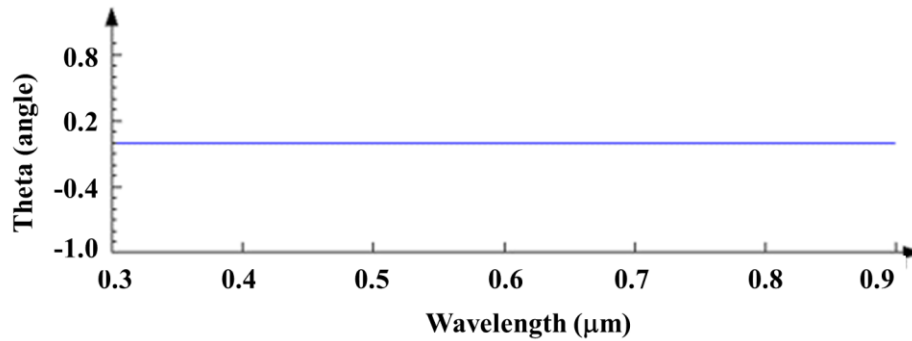


Figure 3.2: Angle of incident light versus wavelength (μm) of the input source parameter for optical analysis.

There are several analysis groups presented in the FDTD solver that return optical results such as the power absorption profile, net power flowing through a box of monitors, quality factor of a resonant cavity mode. With continuous steps of the simulation setup described above, optical results of the device structure can be extracted from the project file.

A periodic plane wave source has been selected as the input parameter to carry out the optical simulations for the solar cell research demonstrated in the following chapters. We have not considered any angle for the incident light shown in Fig 3.2. Figure 3.2 shows that the incident angle is zero for all the wavelength. A periodic/bloch source has been selected, as both the physical structure and the EM fields are periodic. The polarization angle has been considered zero for all the cases. The dimension (x span = $0.4 \mu\text{m}$, y span = $0.4 \mu\text{m}$) of the source has been selected to be the same as the unit cell dimension

considered for all the device structures (x span = $0.4 \mu\text{m}$, y span = $0.4 \mu\text{m}$ and z span = $1.5 \mu\text{m}$). As the injection axis of the plane wave source is in the z-axis, the z-axis position of the source = $1.5 \mu\text{m}$. Note that periodic boundary conditions should be used when both the physical structure and the electromagnetic field are periodic. An error arises when the periodic boundary condition is used while the structure is periodic but the EM field is not. As FDTD is a time domain method, the input signal will be in the time domain (signal versus time) shown in Fig 3.3. Even though FDTD is a time domain method, wavelength/frequency results can be obtained using Fourier Transform in an FDTD solver. This helps to obtain the absorption, reflection, and transmission of a device. By default, the

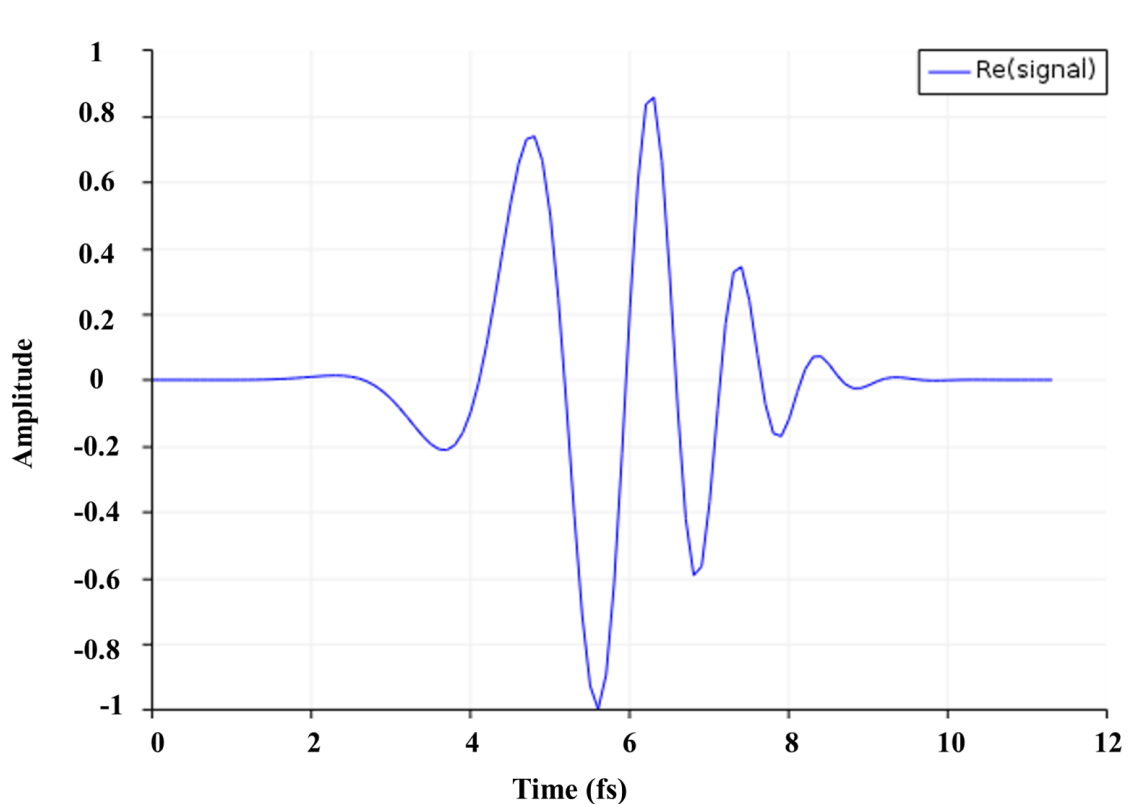


Figure 3.3: Time domain input signal of the plane wave source.

time domain settings are automatically defined to provide the shortest possible pulse. Ideally, we expect the source to inject light at the same intensity for all the wavelengths. For that to happen, it is necessary to use the delta function as a pulse in the time domain. However, since this is not possible numerically, FDTD uses a short pulse. The desired wavelength range is $0.3 \mu\text{m}$ to $0.9 \mu\text{m}$.

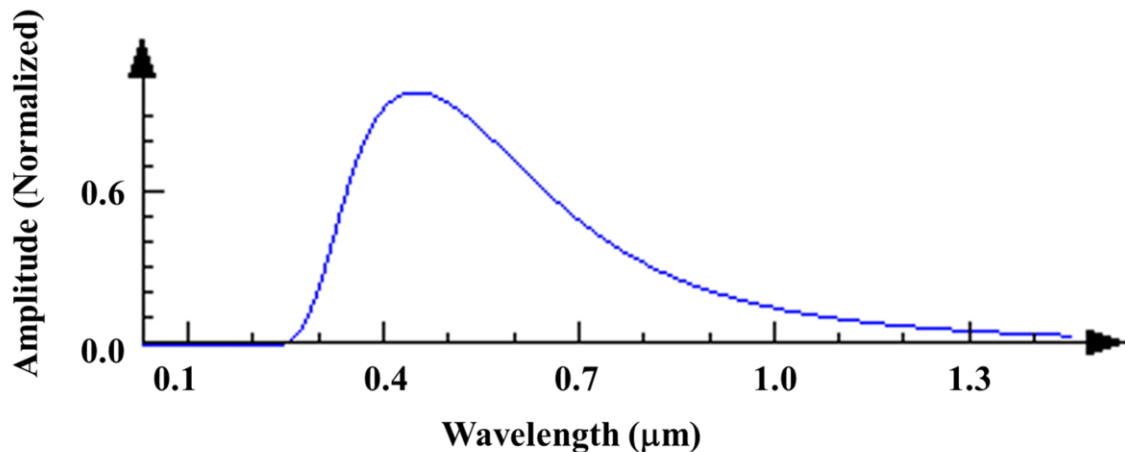


Figure 3.4: Input spectrum of the source in frequency domain (spectrum versus wavelength (μm)). This is the Fourier Transfer of the input time signal.

Even though the wavelength has been confined in a selective range, the source will inject light over a certain range. Note that Lumerical recommends against using a CW source in almost all cases. A CW source will make the data analysis more complicated. In fact, the solver recommends using a broadband pulse. Even if it is required to obtain the response at a single frequency, it is best to use pulse source instead of using CW source. However, CW response (steady state) can be obtained even if a short broadband pulse is used. Fig 3.4 shows the input broadband pulse as a function of wavelength and is the Fourier transform of the input time signal (Fig. 3.3). However, the frequency domain monitors will

automatically generate response of the device within the selective range (0.3 μm to 0.9 μm). By default, the CW normalization option is enabled in FDTD simulations. Here, the CW normalization option has also been used for all the simulation cases to get the response of the system in frequency domain. We must enable CW normalization option, if we intend to obtain results in frequency domain. CW normalization is used to convert the time domain data in frequency (steady state) domain.

3.1.2 Electrical Simulation Solver

In this work, a Charge Transport solver known as CHARGE has been utilized to obtain the electrical performance of the solar cell device. CHARGE solver is an electrical simulation tool widely used in analyzing semiconductor devices [61]. CHARGE is mostly responsible for the distribution of the dopant that creates the electric field inside the device. Moreover, it determines the recombination of the carriers that takes place inside the device. The generation rate profile calculated from the optical solver can be used directly in the electrical solver to determine the responsivity and efficiency of the solar cell.

In addition to that, CHARGE solver has been extensively utilized in steady-state, transient and small-signal analysis of semiconductor devices such as image sensors, photodetectors and modulators. Steady-state solutions are used for the analysis of the system's behavior when time-dependent terms are considered zero and can also be used for the frequency response analysis. CHARGE offers the small-signal AC or SSAC mode for the frequency dependent analysis [61]. On the other side, time-dependent solutions can be used to compute both the transient response of the system and the large-signal response.

Each carrier in the semiconductor device moves due to the drift and diffusion process. Drift of the carrier is caused due to the applied electric field and diffusion due to the gradient of the charge carriers. Hence, Poisson's and drift-diffusion are the main stack of equations solved by the CHARGE solver to determine the density of the free charge carriers and electrostatic potential of the semiconductor device [61]. To solve the drift-diffusion equations of a device, the electric field must be known. The solution of Poisson's equations determines the electric field that is transferred to solve the drift-diffusion equations of the same device. In the entire simulation work, first the optical simulation shows how many of the carriers are generated through the absorption of the optical energy in the semiconductor material (FDTD solver) and then the electrical simulation determines how many of those generated carriers get collected at the contacts and contribute to the output electrical power (CHARGE solver). The Lumerical DEVICE supports various features such as automatic and user-defined mesh refinement which allows the program to attain accurate results while maintaining low memory access. Automatic mesh refinement can be used in the boundaries where there is a sudden change in the properties of the materials (doping and heat generation) within the device. Hence, it helps in computing the entire simulation system while reducing simulation time and memory.

A simple workflow of obtaining electrical results has been illustrated in Fig. 3.5. While setting up a simulation project in DEVICE, it is required to first add materials to the project same as done in the case of the FDTD solver. Electrical properties of the materials are specified in terms of the material models that best describe the charge transport behavior of the materials. Conductor, insulator and semiconductor are three different categorized

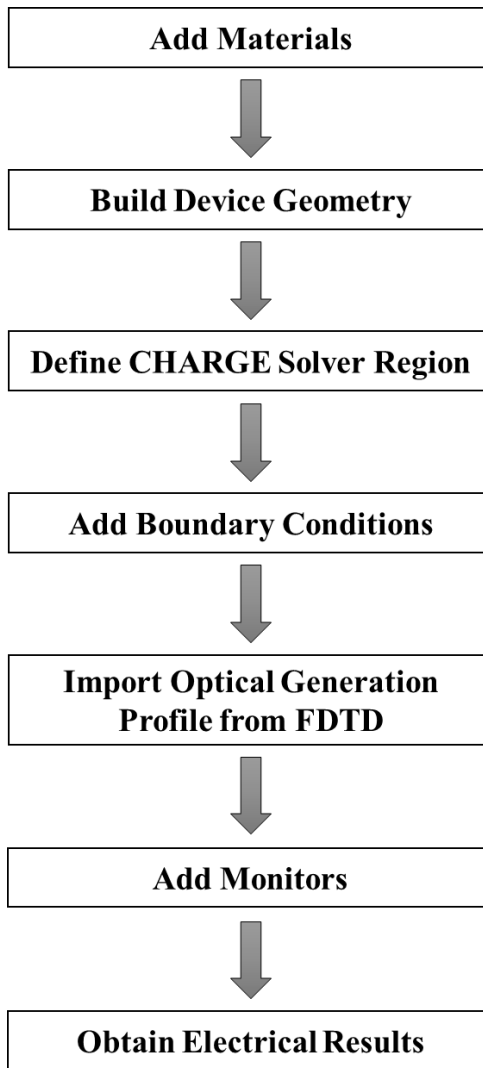


Figure 3.5: Different steps for the electrical simulation process used in the DEVICE module.

materials used in the DEVICE simulation. In addition to that, DEVICE offers various recombination models including trap-assisted recombination, auger recombination and radiative recombination which generate the recombination profile consisting of the number of free carriers available within the device to contribute in the output power. Building the structure of the device with various structure primitives (*e.g.* rectangle, circle, triangle) which are available in DEVICE is the second step to continue with the simulation work.

Complex geometries can also be modified with the knowledge of the scripting language as mentioned in the FDTD solver section. CHARGE simulation region sets the dimension (x span = 0.4 μm , y span = 0.4 μm and z span = 1.5 μm) of the unit cell of the simulation area and it has to be the same as chosen in FDTD solver. Any structure or object outside the simulation region doesn't take part in the simulation. Through the entire electrical analysis of the project, the CHARGE solver has been specified to steady-state and isothermal analysis. CHARGE solver consists of several other features that includes doping of the device and adding boundary conditions. However, doping is only valid for the semiconductor materials. Conductors and insulators do not require any doping for the simulation. The available doping options that can be superimposed on the solar cell structure includes constant doping, diffusion doping, and implant doping. For our research work, constant doping has been utilized to define the regions under study.

The boundary condition group consists of electrical and surface recombination boundary conditions which are under the CHARGE solver region. Electrical boundary conditions are used to apply small-signal, DC or transient voltage to the electrical top and bottom contact which are used for the collection of the free carriers. These boundary conditions allow the user to define the bias voltage and surface recombination velocity. Electron and hole pairs recombine due to the impurity trap states at the surface. Surface recombination models available in the CHARGE solver are utilized for the computation of the recombination of the carriers at the surface. Interface recombination between two different materials can also be applied using this boundary condition. Importing the optical generation profile that has been generated using the FDTD solver is the most important part in the electrical

stimulation of the device. Charge monitors, electric field monitors, band-structure monitors, current flux monitors can be applied to (i) record the electron and hole densities (ii) compute electric field and electrostatic potential (iii) depict the equilibrium band structure (iv) calculate total flux of the current density (respectively) within the monitor region specified. Thus, this step by step procedure will allow a user to obtain the electrical response of the system in the DEVICE module.

3.2 Properties of ZnO and ZnTe

For accurate simulations, it is necessary to match the physical properties of the associated materials with the parameters of the models. Both optical and electrical parameters need to be matched and calibrated before performing the simulations for the solar cell. This section provides details on the calibration and property matching procedure.

3.2.1 Optical Properties

To create new materials for the simulation from the measured experimental data, sampled 2D or sampled 3D models are utilized in FDTD. Measured experimental data cannot be used directly in the simulation file; as a result, a sampled data-base material model can be used to define the materials based on the experimental values of the real and imaginary part of the refractive index (n, k). Even if the automatically generated analytical model does not fit well, it can be adjusted using fit tolerance and max co-efficient parameters [62].

This section will describe how new materials can be added into the Material Database and how to check the material fit with the Material Explorer. Before starting the simulation, the user must check the fitting of the material with the help of the Material Explorer. If it is not well fit, then the fitting of the material is required to ensure proper outcomes. The material database of the FDTD solver supports several material permittivity models. However, sampled 3D data model has been utilized to create new materials for the simulations for our project as it is more recommendable than the sampled 2D data model which is also available in the material database. While creating sampled 3D data type material, the experimental data of the material should be saved in a text file of three columns where the first column contains the wavelength or frequency, second and third column contain the real and imaginary part of the refractive index (n , k) of the material respectively.

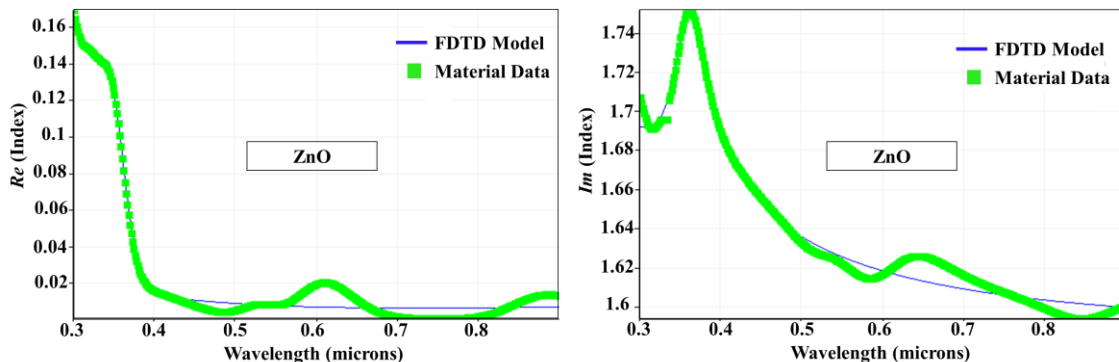


Figure 3.6: Fitting of real and imaginary components (n , k) of the refractive index for ZnO with Material Explorer.

ZnO and ZnTe material fitting has been performed with the ‘Material Explorer’ component of the FDTD solver. ZnO and ZnTe materials are the main material systems used for the design of the solar cell in this work. First, wavelength versus refractive index plots are automatically generated using the experimental (n , k) values of ZnO and ZnTe material

[62]. The blue curves in Fig. 3.6 and 3.7 represent outputs using the FDTD model. The green curves in Fig. 3.6 and 3.7 represent the plots obtained using experimental (n, k) values. To fit the green curve and the blue curve (for each case), max coefficient parameter has been adjusted for both the material. Max co-efficient refers to the number of maximum co-efficient allowed in the model. An excessive number of coefficients results in higher sensitiveness of the fitting to the noise present in the experimental data. In addition, lower co-efficient gives significant error in the fitting. As a result, an adjustment of the co-efficient parameter in fitting the material data is essential. By default, max-coefficient of 6 is used for the sampled data model. Hence, these matched parameters (Fig 3.6 and Fig 3.7) have been used for the subsequent simulations.

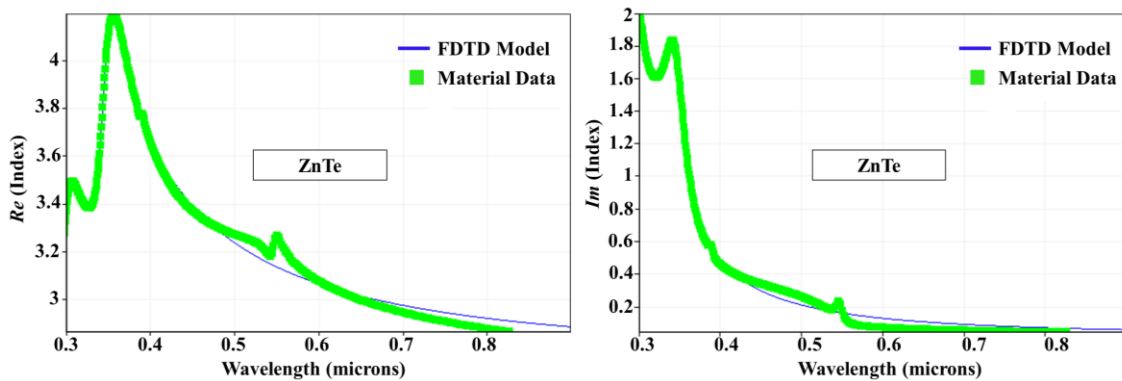


Figure 3.7: Fitting of real and imaginary components (n, k) of the refractive index for ZnTe with Material Explorer.

3.2.2 Electrical Properties

Fundamental electronic properties of a semiconductor material are required to create a new material model in the Material Database of DEVICE. These basic electronic properties define the electrical behavior of a semiconductor material. The electrical properties of ZnO

and ZnTe materials are shown in Tables 3.1 and 3.2. Some of the parameters have been obtained from literature and some have been calculated using physical equations. These electrical properties of the materials define the charge transport behavior. Therefore, these electrical parameters have been used to update the existing material database by creating new materials as required for the simulations.

Table 3.1: Electrical Properties of ZnO

DC Permittivity [63]	9
E_c Valley [64]	γ
Electron effective mass	$0.248m_0$
Hole effective mass	$0.801m_0$
Bandgap (eV) [65]	3.3
Electron Mobility ($\text{cm}^2/\text{V-s}$) [66]	100
Hole Mobility ($\text{cm}^2/\text{V-s}$) [66]	31

Table 3.2: Electrical Properties of ZnTe

DC Permittivity [67]	7.4
E_c Valley [68]	γ
Electron effective mass	$0.129m_0$
Hole effective mass	$0.599m_0$
Bandgap (eV) [67]	2.24
Electron Mobility ($\text{cm}^2/\text{V-s}$) [67]	340
Hole Mobility ($\text{cm}^2/\text{V-s}$) [67]	100

3.3 Structural Comparison of Device Models

Two different geometrical designs of the solar cell have been investigated in this research. One is very common; the planar structure and the other is the cylindrical pillar structure. The conventional thin film solar cell structure is already popular among the solar research

community. However, exploration of microstructure or nanostructure such as micropillar, nanorods and quantum dot structures are growing rapidly in the research community because of their high efficiency and low-cost capability [69]. Radial (core-shell) and axial junctions are two types of micropillar solar cell (discussed in chapter 2) [70]. This section details these variants of solar cell with specific focus on ZnO/ZnTe material system.

3.3.1 Structural details of Planar ZnO/ZnTe Solar Cell

The combination of ZnO and ZnTe (both II-VI) is one of the most studied types of concurrent solar cells because of its non-toxicity and high absorption capability [28]. ZnO and ZnTe have a bandgap of 3.3eV and 2.24eV respectively. In the planar geometry presented in Fig. 3.8, ZnO is the emitter layer and ZnTe is the absorber layer mounted on Al doped ZnO transparent metal oxide substrate (AZO). Cu has been used as the top metal contact for the collection of the free carriers. At present AZO is being widely used as a metallic layer for carrier transport [71]. Though Indium tin oxide (ITO) is the most popular transparent conductive oxide, it is highly toxic and scarcer [72]. As a result, the invention of an alternative material to Indium tin oxide (ITO) is of intense research interest. Therefore, AZO can be considered as an alternative to the ITO because of its high stability, abundance and lower cost compared with ITO [72]. Surface work function of AZO material can be between 3.7 eV to 4.4 eV [71].

One electrical unit cell (x span = 0.4 μm , y span = 0.4 μm and z span = 1.5 μm) has been considered to obtain the computational results of the planar ZnO/ZnTe solar cell from the DEVICE simulator. The thickness of ZnTe and ZnO layer is 1.0 μm and 0.5 μm

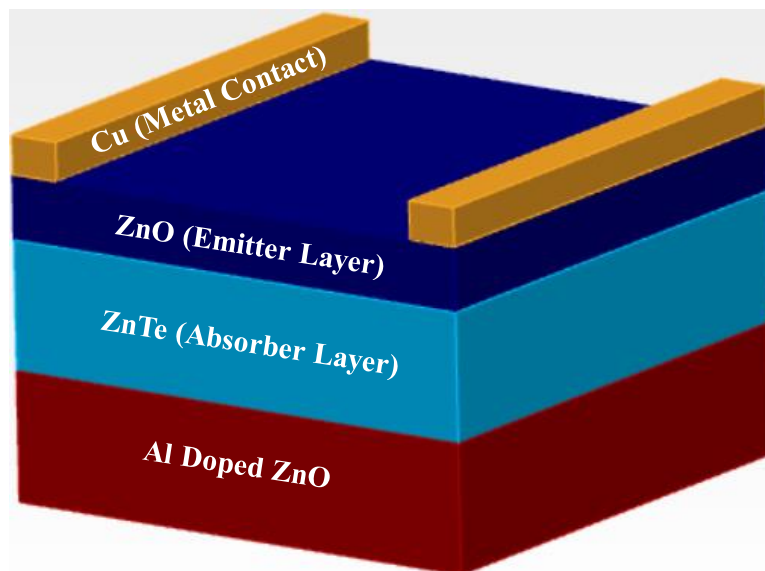


Figure 3.8: One electrical unit cell of a planar ZnO/ZnTe solar cell. Different layers of materials have been annotated on the schematic.

respectively. In total, the height of the entire solar device is $1.5 \mu\text{m}$ excluding the thickness of AZO (bottom contact). The thickness of AZO ($2 \mu\text{m}$) for all other structures (radial and axial micropillar, bottom contact) has been considered the same. The energy band-diagram

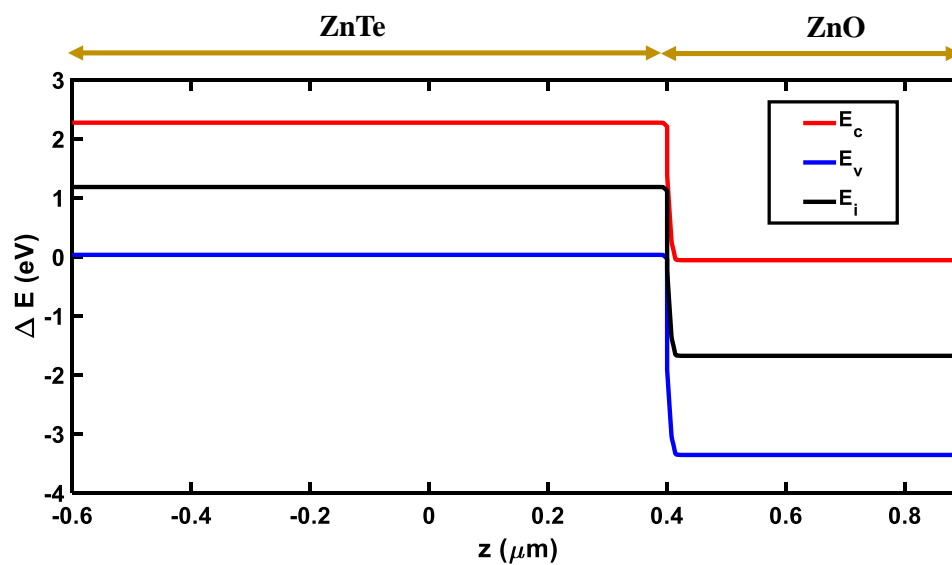


Figure 3.9: Energy band-diagram for conventional ZnO/ZnTe solar cell. Bandgaps for ZnTe and ZnO are 2.24 and 3.3 eV, respectively.

of ZnO/ZnTe solar cell has been depicted in Fig. 3.9 which is obtained by the band-structure monitor. ZnO/ZnTe solar cell has a high charge separation efficiency because of its band alignment [28]. In fact, the band-alignment can even be modified by the strain between two materials that depends on the growth time [73].

3.3.2 Structural Details of ZnO/ZnTe Micropillar Solar Cell

The pillar structure provides potential advantages over the planar structure. The main advantages of pillar-based solar cell include reduction in reflection of light, light trapping potential, bandgap tuning and increased defect tolerance [74]. Over the years, the research in micropillar or nanowire structure has drastically taken the attention. At the same time, development in the manufacturing sector has improved tremendously which increased the possibility of manufacturing high-performance electronic devices. Based on the junction, the pillar-based solar cell can be divided into two types such as radial junction and axial junction [70]. The cross-sectional view of radial and axial junction ZnO/ZnTe micropillar

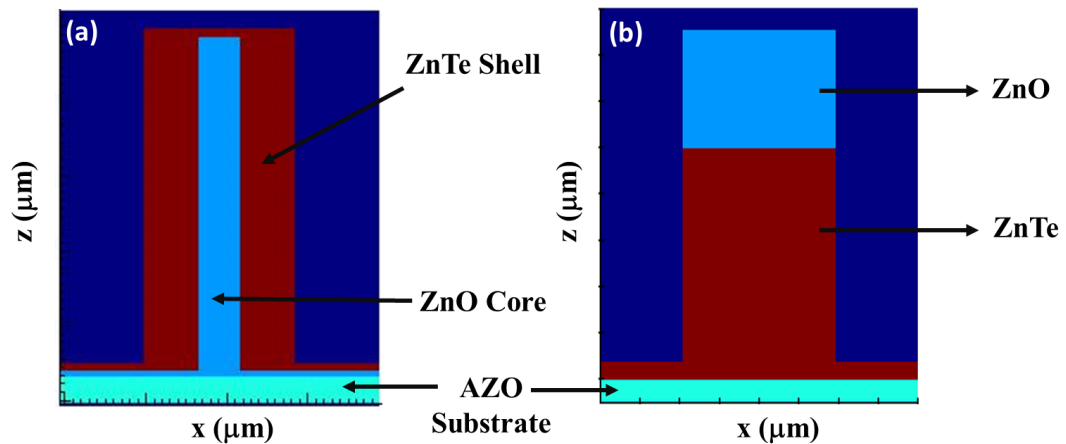


Figure 3.10: One single pillar of (a) radial junction ZnO/ZnTe micropillar solar cell and (b) axial junction ZnO/ZnTe micropillar solar cell.

solar cell has been shown in Fig. 3.10. The height of both of the pillars are kept to $1.5 \mu\text{m}$ to compare its computational outputs with the conventional ZnO/ZnTe micropillar solar cell of $1.5 \mu\text{m}$. In order to facilitate direct comparison between radial and axial junction, both radial and axial junction pillars of the solar cell are of same diameter and height. The blue color (background region) represents the air.

- *Axial Junction ZnO/ZnTe Solar Cell*

The Axial junction is a type of micropillar solar cell that has some advantages over the planar geometrical structure. The direction of the incident light and the carrier collection are identical with the planar device. The direction of the incident light is in the z direction. Merely the periodic pillar architecture provides reduction in the light reflection and enhances the light trapping possibilities. Optimization of the pillar dimension might enhance the light trapping and absorption properties. Fig. 3.11 illustrates the schematic of axial junction ZnO/ZnTe micropillar solar cell where the red portion is the ZnO material

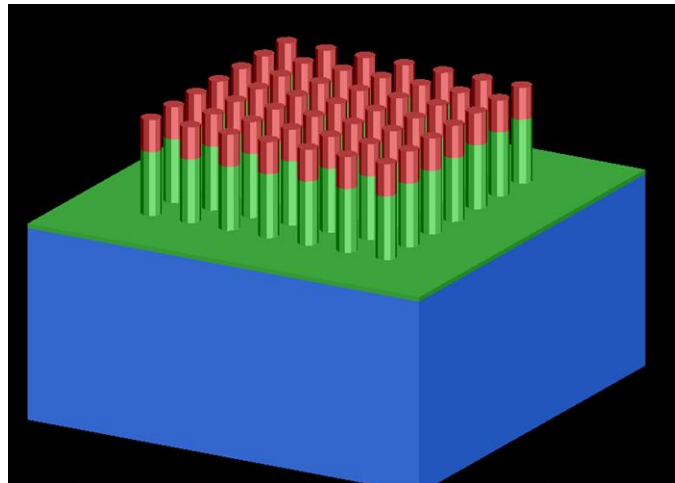


Figure 3.11: 3-D Schematic of ZnO/ZnTe axial junction (core-shell) micropillar array solar cell.

and the green portion is ZnTe absorber material. A simple etching process of a planar ZnO/ZnTe solar cell can create this axial junction pillar architectural design [75]. The top red portion of the pillar (ZnO) is of 0.5 μm and the bottom part of the pillar (ZnTe) is of 1 μm . In total, the height of the pillar is 1.5 μm for the computational comparison, as mentioned before. Also the diameter (95 nm) of the axial pillars of this solar cell are identical to that of radial junction solar cell.

The bottom contact on which the pillars are mounted is Aluminium doped ZnO material (AZO). The top contact (Cu) has been placed on top of the pillars for our simulation project. Ideally, the top contact can be placed all over the pillar body or only on top of certain number of pillars rather than covering the entire top of the pillars [76]. However, the limitation of the solver leads to higher simulation time and memory space for such top contact design. For most of the cases in Lumerical Device (examples), the top contact has been placed on top of the entire pillar structure of the solar cell. Therefore, to make the computational process easier, the top contact has been kept on top of the pillars for all of our project files. Generation rate of the carriers that has been obtained from the FDTD simulation is imported in DEVICE to carry out the electrical performance analysis further.

Radial Junction ZnO/ZnTe Solar Cell

In the radial junction ZnO/ZnTe solar cell, analyzed in this work, the direction of incident light and carrier collection are orthogonal. So the pillars can be as long as it is required to absorb all the incident light and the radius needs to be thinner than the diffusion length of

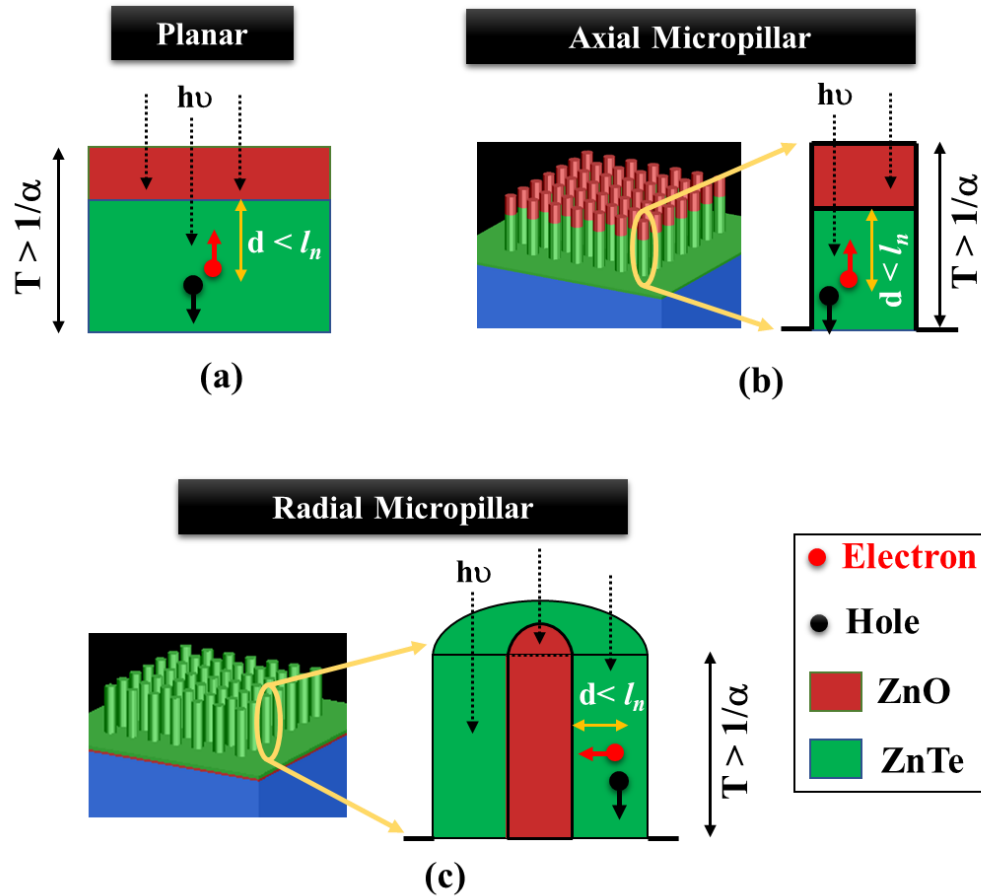


Figure 3.12: Scenario of light absorption and charge transport in (a) planar ZnO/ZnTe solar cell (b) axial micropillar ZnO/ZnTe solar cell and (c) radial (core-shell) micropillar ZnO/ZnTe solar cell.

the minority carriers to collect all the generated carriers. The top (Cu) and bottom contact (AZO) is similar to that of the axial junction pillars which is discussed in the above section. Fig. 3.12 shows the collection of carriers in a planar device (Fig. 3.12 (a)) and in the other two types of micropillar structures (Fig. 3.12 (b), (c)). Fig. 3.12 (c) shows the schematic of ZnO/ZnTe core-shell array micropillar solar cell of $1.5 \mu\text{m}$ in height. The core is comprised of n-type ZnO material and the shell is p-type ZnTe material. The diameter of the core is

limited to 50 nm and the thickness of the shell is limited to 70 nm for the subsequent simulations.

Optical thickness or optical depth ($1/\alpha$) is the measurement of the attenuation of the transmitted light through a material. If the device is as thick as the optical thickness, about 90% of the incident light can be absorbed. To absorb all of the incident light, the following condition needs to be met-

$$T > (1/\alpha) \tag{3.1}$$

Here, T is the thickness of the device.

To collect the generated carriers, the minority carrier diffusion length ($l_{n/p}$) must be greater than the distance that the generated carriers travel before getting collected. The carriers that are generated near the junction, can be easily collected by the electric field across the junction. Collection becomes problematic and difficult when the generation occurs towards the bottom part of the device. To collect these carriers with highest possible efficiency, the following condition needs to be satisfied-

$$l_{n/p} > (1/\alpha) \tag{3.2}$$

In a planar ZnO/ZnTe device (Fig. 3.12 (a)), it becomes very difficult to fulfil the above stated requirement. A thick absorber layer is required to meet the condition in (3.1). In order to ensure efficient carrier collection in a planar device, highly crystalline and pure materials are required [78]. That leads to higher material cost.

In the case of the axial micropillar structure (Fig. 3.12 (b)), the restriction on thickness for carrier collection is similar to that in the planar structure. This structure suffers from the same problem of collecting carriers from the bottom part of the pillars. As a result, no benefits are obtained by using axial micropillar in terms of carrier collection. But, due to the unique geometry of the pillar structure, absorption efficiency increases and reflection reduces.

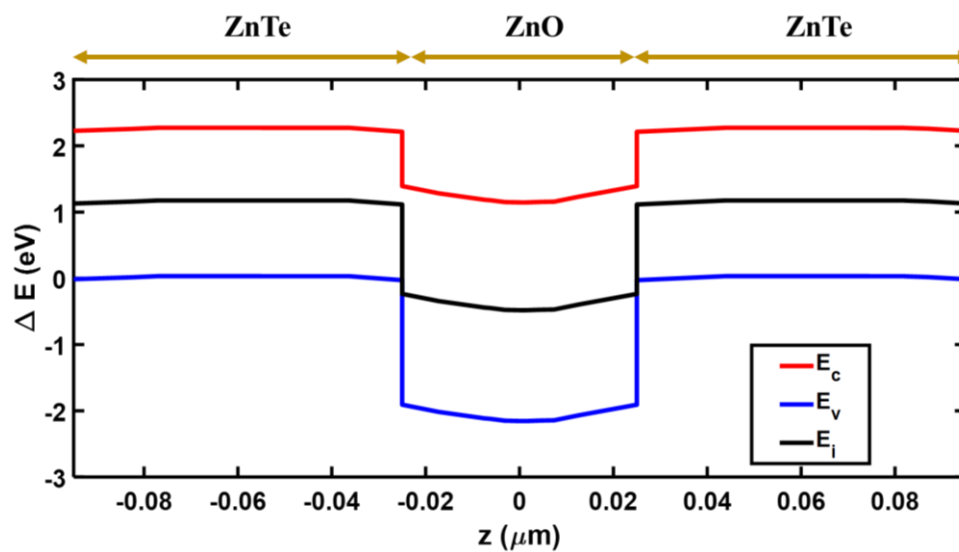


Figure 3.13: Energy band-diagram for a radial micropillar ZnO/ZnTe solar cell. Bandgaps for ZnTe and ZnO are 2.24 and 3.3 eV, respectively.

On the other hand, due to the orthogonal nature of light absorption and carrier collection, the radial micropillar structure (Fig. 3.12 (c)) is not limited by the condition (3.2). The minority carriers have to travel the same radial distance to get collected, irrespective of their depth inside the pillar. Hence, the pillars can be made as large as possible (to absorb more light), without hurting the collection efficiency. In addition, it renders the same benefit of higher absorption due to its geometry, as the axial micropillar. Thus a radial

micropillar structure provides a unique opportunity to realize a low-cost and efficient solar cell. Fig. 3.13 represents the band-diagram of the radial ZnO/ZnTe micropillar solar cell.

3.4 Results and Discussion

In this section, simulated results for the optical and electrical analysis will be presented for all of the device structures (planar, axial micropillar and radial micropillar) discussed in the previous section.

3.4.1 Optical Analysis

Optical analysis evaluates the reflection, transmission and absorption ability of a device. Efficient solar cell requires less reflection and higher absorption of the incident light. Fig. 3.14 (a, b and c) show the comparison of the reflection, transmission and absorption between planar, axial junction and radial junction ZnO/ZnTe micropillar solar cells. The light range used for the optical analysis is in the range of 0.4 μm to 0.7 μm . The reflection shown in Fig 3.14(a) demonstrates that planar ZnO/ZnTe has higher reflection compared to both micropillar ZnO/ZnTe solar cells. However, the planar structure has lower reflection in the range of 0.6 μm to 0.7 μm . But the transmission of this planar device is higher in the range between 0.6 μm to 0.7 μm as shown in Fig 3.14(b). Therefore, the overall absorption of a planar device is lower as shown in Fig 3.14. This directly corresponds to the following relation-

$$A=1-R-T \tag{3.3}$$

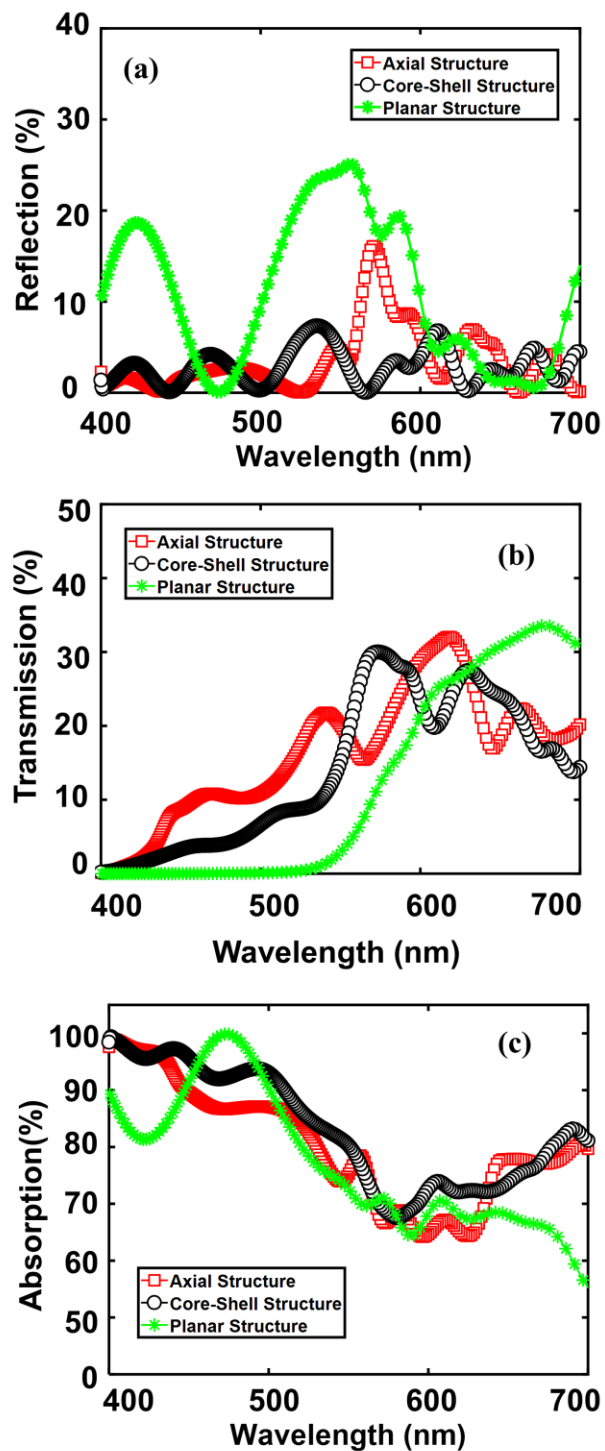


Figure 3.14: Comparison of (a) reflection (b) transmission and (c) absorption in three different solar cell structures (planar, radial micropillar and axial micropillar).

Where, A = Absorption

R = Reflection

T = Transmission

Fig 3.14(c) depicts that absorption of the ZnO/ZnTe micropillar solar cells increases in the higher wavelength region compared to the planar structure. In fact, the reflection of radial junction ZnO/ZnTe micropillar solar cell is lower nearly in the entire range of incident light shown in Fig. 3.14 (a). In addition to that, the transmission of radial junction solar cell is lower than the other two device structures except within a small range (0.55 μm to 0.59 μm).

Thus, the optical analysis shown in Fig 3.14 illustrates lower reflection and higher absorption in radial junction ZnO/ZnTe micropillar solar cell compared to the other two structures. It is because of its pillar-based device structure. Hence, it is supposed to generate maximum number of carriers. The generation profiles of all the device structures are presented below.

3.4.2 Carrier (Electron-Hole Pairs) Generation Profile

The generation profiles provided in this section will illustrate the degree of carrier generation in response to the absorption of the incident light. The purpose of this analysis is to find the region with most levels of carrier generation and the zones that do not generate any carriers at all. Note that the corresponding color bar with each figure (Fig. 3.15 and

3.16) represents the relative levels of carrier generation in log scale ($\log_{10}(G)$). Here, G (unit = charge pairs/ m^3/s) refers to the generation of the carriers. The color red and blue represent high and low levels of generation respectively.

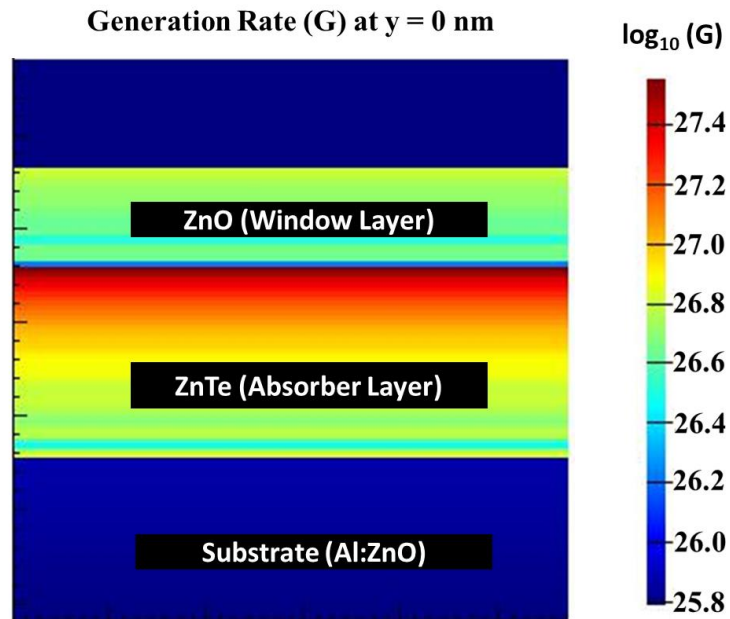


Figure 3.15: Carrier generation profile for planar ZnO/ZnTe solar cell. The respective layers have been marked in the above figure.

The generation profile for planar ZnO/ZnTe solar cell is shown in Fig. 3.15. As the red color covers the upper portion of the ZnTe absorber layer (near the junction area), it indicates maximum carrier generation in that particular region. The mixed yellow and green in the emitter ZnO layer reports lower carrier generation as ZnO has higher bandgap (3.3 eV). Moreover, lower generation is observed in the bottom part of the absorber layer of the planar ZnO/ZnTe solar cell. However, it has been assumed that for every photon energy absorption, one pair of electron and hole is generated irrespective of the material

(Lumerical FDTD solver). Moreover, charge solver only solves the drift and diffusion equation for the semiconductor materials, as a result, generation of carriers in metals and insulators are not of any concern. The color bar only represents the carrier generation profile of the ZnO and ZnTe materials.

Fig. 3.16 (a - c) illustrate the generation profile for the axial junction ZnO/ZnTe micropillar solar cell. Observing from different planes of cross-sections (XZ, YZ, XY), it is apparent

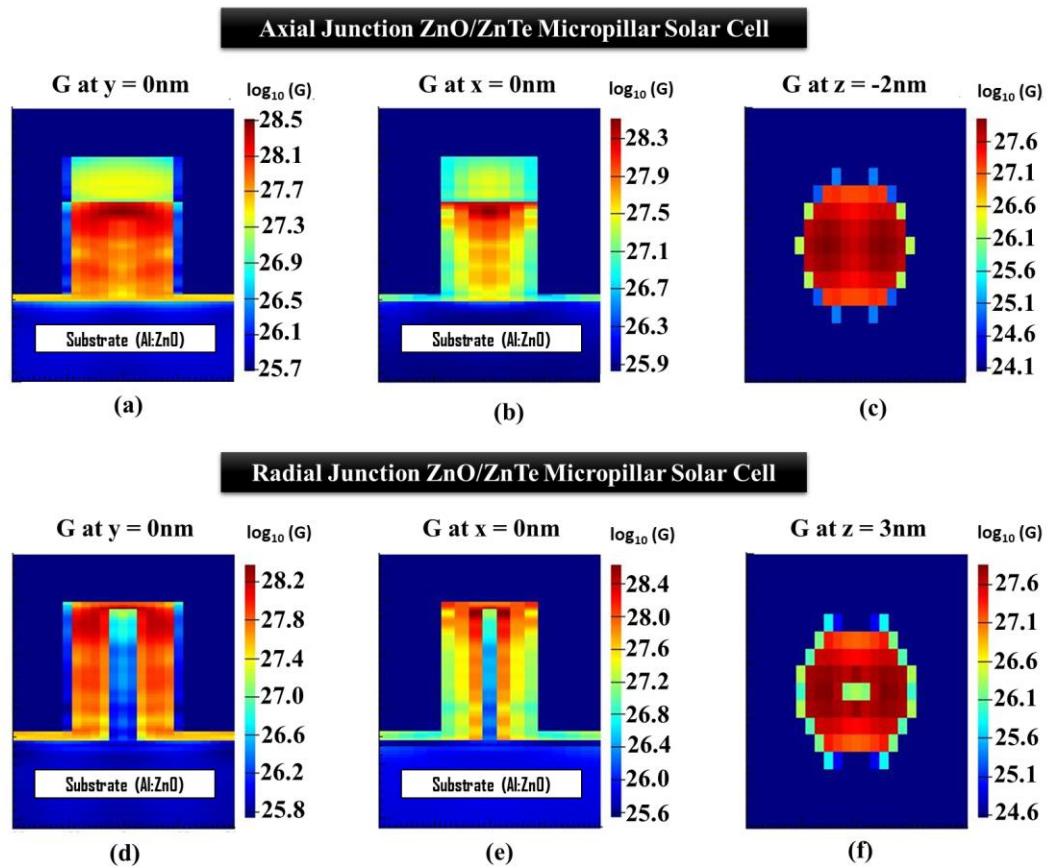


Figure 3.16: Generation profile for axial junction ZnO/ZnTe micropillar solar cell, observed from (a) XZ plane (b) YZ plane and (c) XY plane at 2 nm depth. (d-f) Show similar generation profiles for radial junction ZnO/ZnTe micropillar solar cell, observed from (d) XZ plane (e) YZ plane and (f) XY plane at 3 nm depth.

that the generation profile is similar to that of the planar structure. From the color code, it is clear that most absorption occurs near the junction. Interestingly, significant amount of absorption is also observed towards the bottom part of the pillar (unlike in planar). That demonstrates the advantage of the micropillar geometry. From the XY plane at 2 nm depth, the generation appears to be uniformly distributed across the circular area.

On the other hand, Fig. 3.16 (d - f) show the generation profile for radial junction ZnO/ZnTe micropillar solar cell. The generation profile for this case is very different compared to the planar and axial micropillar versions. There appears to be almost very less carrier generation inside the ZnO core. Most of the carrier generation occurs within the shell ZnTe layer. Vertically, a generation is almost identical throughout the shell layer, with the bottom part having slightly lower concentration of generated carriers (Fig. 3.16 (d)). From the XY plane at 3 nm depth, the generation appears to be highly concentrated towards the circumference and lower towards the center. That shows the radial nature of the carrier generation.

3.4.3 Electrical Analysis

Fig. 3.17 shows the simulated electrical characteristics of ZnO/ZnTe solar cells. Fig. 3.17 (a) and (b) show the comparative current density and power density curves respectively. They illustrate that the axial junction micropillar cell has lowest current and power density among the three structures in consideration. Even though, its optical performance is better than that of the planar structure (discussed before), the collection efficiency shows the opposite trend. The reason is that, in an axial micropillar structure, the junction area per

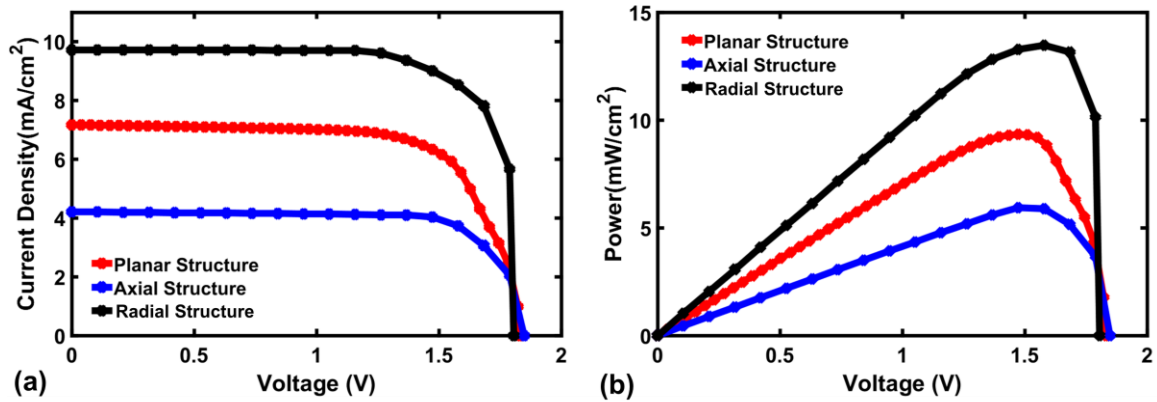


Figure 3.17: (a) Current-voltage (I - V) and (b) Power-voltage (P - V) characteristics for different structures (planar and micropillar) of ZnO/ZnTe solar cell.

pillar is small compared to a continuous planar structure. Although the total area of all the junctions in the array will add up to the area of the planar solar cell (as per simulation set-up), due to the discontinuity, the collection area becomes lower. Therefore, the current density and power density suffers. Note that the input power (P_{IN}) was considered to be 1000 W/m^2 . On the contrary, in a radial structure, not only the generation area but also the collection area is large. Hence, the electrical performance gets enhanced in compliance with the optical performance. Among all of these structures, the radial ZnO/ZnTe micropillar solar cell can achieve up to a current density of $\sim 10 \text{ mA/cm}^2$ and power density of $\sim 14 \text{ mW/cm}^2$.

3.5 Summary

Based on the analysis of optical response, electrical performance, and carrier generation profile, it is clear that the radial micropillar ZnO/ZnTe solar cell has clear advantages over

the other two (planar and axial micropillar) structures. The comparative results (obtained from the FDTD solver) are summarized in Table 3.3.

Table 3.3: Performance Comparison for Different Structures of ZnO/ZnTe Solar Cell.

Structure	Ideal J_{SC} (mA/cm ²)	Ideal G_{MAX} (m ⁻³ s ⁻¹)
Planar	21.37	3.83×10^{27}
Axial Micropillar	22.05	3.27×10^{28}
Radial Micropillar	24.47	4.27×10^{28}

Axial micropillar structure has higher ideal short circuit current (J_{SC}) (22.05 mA/cm²) and larger ideal maximum generation (G_{MAX}) (3.27×10^{28} m⁻³s⁻¹) compared to the planar structure. However, due to having lower collection area, the axial micropillar structure incurs lower efficiency. However, the radial junction solar cell has highest J_{SC} (24.47 mA/cm²) and G_{MAX} (4.27×10^{28} m⁻³s⁻¹) among all three of the structures under consideration. Therefore, this structure is the best choice for solar cell design with ZnO/ZnTe materials. In the subsequent chapters, this radial ZnO/ZnTe micropillar solar cell structure will be further analyzed to examine the effect of the doping profile and its dimension (height, pitch, and diameter).

CHAPTER 4

IMPACT OF DOPING ON A ZnO/ZnTe MICROPILLAR SOLAR CELL

This chapter presents the effect of doping on the performance of a radial micropillar ZnO/ZnTe solar cell. First, the effect of doping levels on open circuit voltage (V_{oc}), short circuit current density (J_{sc}), fill factor and efficiency is analyzed. Next, the impact of auger recombination is investigated.

4.1 Effect of Doping on Electrical Parameters

The open circuit voltage (V_{oc}) does not change significantly with an increase in doping concentration (within 1×10^{18} - 3×10^{19} cm^{-3}). This trend can be explained by recalling equation (2.1). V_{oc} is logarithmically dependent on doping concentration and hence very less responsive to changes in the latter. Fig. 4.1 (a) illustrates this trend, where the V_{oc} appears to remain close to 1.8 V even for more than an order of magnitude change in doping concentration.

The short circuit current density (J_{sc}) decreases with increase in doping concentration, as shown in Fig. 4.1 (b). For a doping concentration of 2×10^{19} cm^{-3} , the J_{sc} falls below 10 mA/cm^2 . The reason for degradation in J_{sc} is the increased levels of auger recombination resulting from higher carrier concentration [79]. A high level of recombination reduces the amount of collected carriers and thereby reduces the current density. This effect is discussed in detail in the next section.

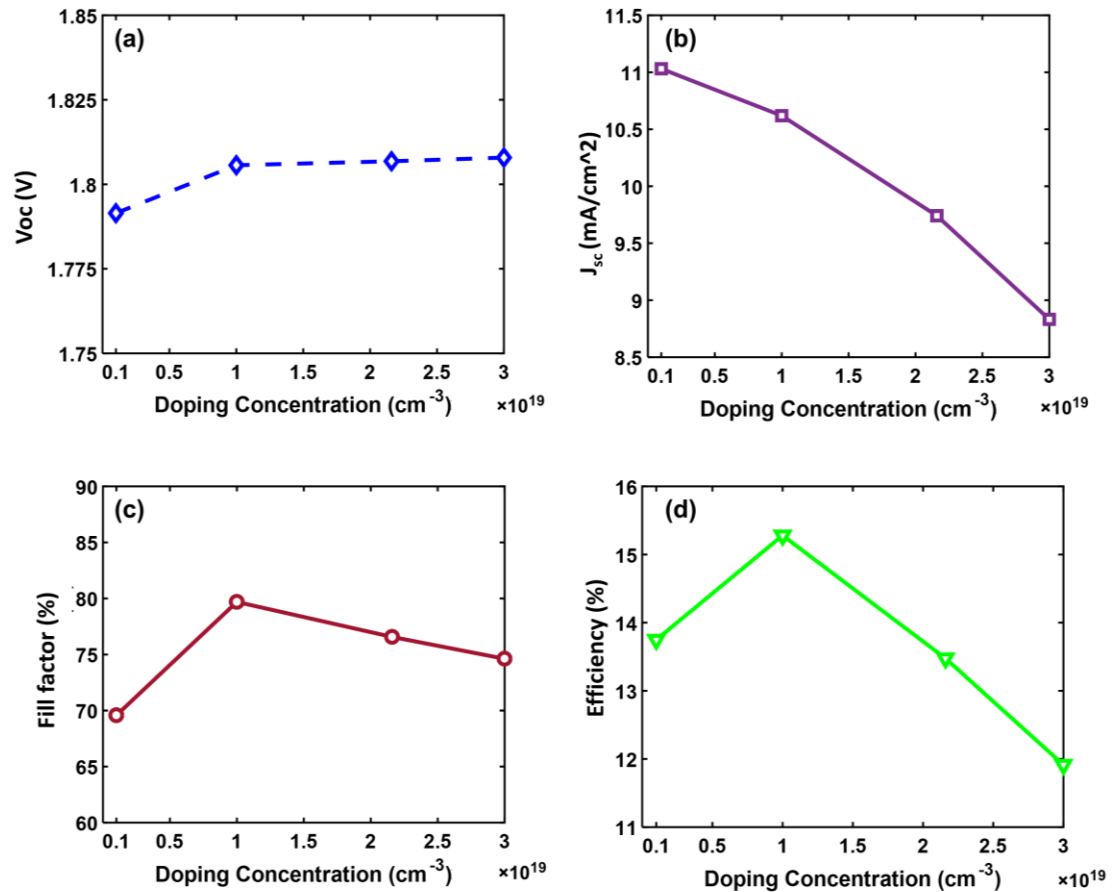


Figure 4.1: Effect of doping concentration on the (a) V_{oc} (b) J_{sc} (c) Fill factor and (d) efficiency of a radial micropillar ZnO/ZnTe solar cell.

The fill factor (FF) and efficiency (η) show non-linear trends with respect to the doping concentration (Fig. 4.1 (c), (d)). Clearly, the values of FF and η reach a peak value for a doping concentration of $1 \times 10^{19} \text{ cm}^{-3}$. For doping concentrations higher or lower than $2 \times 10^{19} \text{ cm}^{-3}$, both of these parameters (FF and efficiency) get degraded. The cause is the interplay between the degree of carrier generation and the amount of recombination. For lower doping concentrations, the carrier concentration is lower. That leads to lower FF and η . Even though the recombination rate is also very low with lower doping concentrations,

the carrier concentration becomes the dominant factor. On the other hand, for higher doping concentration, recombination becomes the dominant component, increasing significantly for higher doping concentration. Such high level of recombination leads to degraded FF and η . Considering both of these factors, the optimum values of FF and η occur when the maximum amount of carrier concentration is achieved with as low a level of recombination as possible.

4.2 Effect of Auger Recombination

Three common types of recombination occur in a photovoltaic device that result in reduction of the concentration of collected carriers. Radiative, schockley-read-hall, and auger are the three common recombination phenomena. In particular, auger recombination, a carrier-carrier interaction process, takes place where the concentration of carriers is high [79].

In the auger recombination process, electron-hole pairs recombine and transfer their energy to another carrier in a non-radiative process, thus increasing the kinetic energy of the carrier. Theoretical and experimental efforts have been made to understand the auger recombination in nanostructures [80]. It has been reported that auger recombination in micro or nanowires can be called two-particle collision rather than three particle collision [80].

Increase in the dimension of nanostructure has been reported to aid in suppression of the auger recombination process [80]. The auger capture rates have been claimed to depend on

the size and the geometry of the quantum dots [81]. Yah He [80] reported that the auger lifetime logarithmically increases with the diameter of nanowires . It is challenging to understand the effect of geometry parameters on the auger recombination process. Mathematically, auger recombination rate (R_A) can be expressed as-

$$R_A = C_A \times n^3 \quad (4.1)$$

Here, C_A is the auger co-efficient and n denotes carrier concentration.

Auger recombination decreases strongly with the increase in bandgap [82]. As a result, the wide bandgap materials are less affected by auger recombination. One research states that the auger co-efficient is to be on the order of $1 \times 10^{-30} \text{ cm}^6 \text{ s}^{-1}$ [82], while other researchers indicate significantly higher values ($1 \times 10^{-27} \text{ cm}^6 \text{ s}^{-1}$ to $1 \times 10^{-24} \text{ cm}^6 \text{ s}^{-1}$) [82].

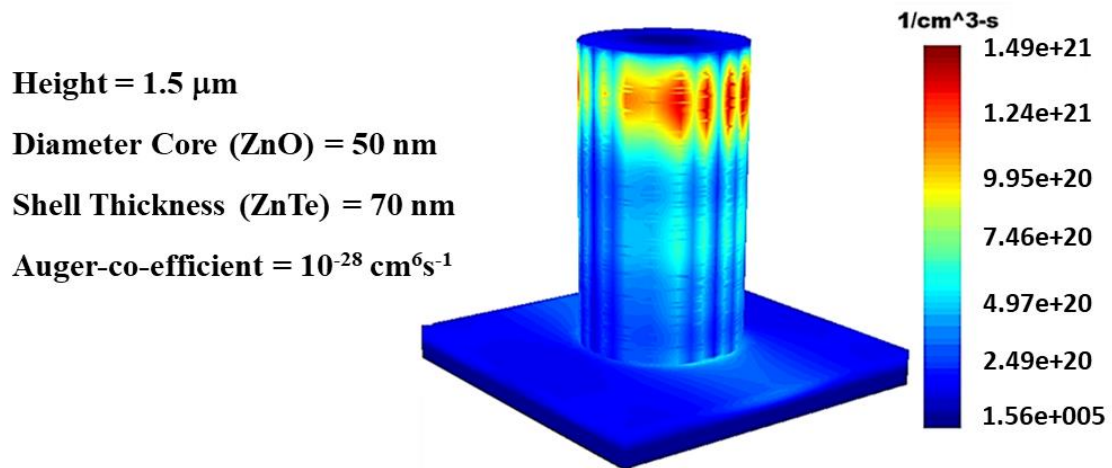


Figure 4.2: Auger recombination profile for radial core-shell micropillar ZnO/ZnTe solar cell of 1.5 μm height.

Figure 4.2 shows the auger recombination rate at different locations of a radial ZnO/ZnTe micropillar solar cell. The red and blue portions of the color spectrum represent high and

low levels of auger recombination rate respectively. Clearly, the auger recombination rate is highest towards the tip of the micropillar. The reason is that the top portion of the micropillars have the highest amount of generation (recall Fig. 3.16 (d)) and therefore high level of photo-generated carriers. High carrier concentration leads to a higher probability of recombination.

The efficiency of the ZnO/ZnTe radial micropillar solar cell is affected by the level of doping concentration as well as the auger co-efficient. To investigate the correlation, this work explores different levels of doping concentration for the ZnTe shell with the ZnO core being fixed at a concentration of $1 \times 10^{19} \text{ cm}^{-3}$. Figure 4.3 shows the results of this analysis. Clearly, higher auger co-efficient leads to lower efficiency as the higher auger co-efficient means higher auger recombination (recalling 4.1). Significant degradation is observed in efficiency for values of auger co-efficient beyond $1 \times 10^{-28} \text{ cm}^6 \text{ s}^{-1}$. However, the effect of auger recombination is only seen for higher doping concentration (greater than

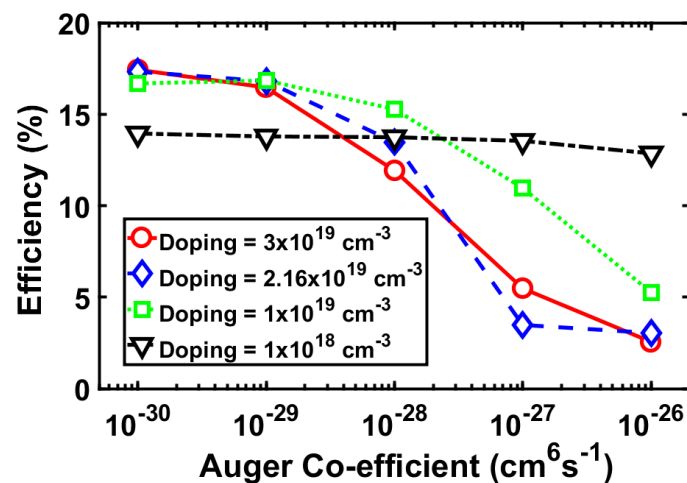


Figure 4.3: Effect of different degree of Auger recombination and doping levels on the efficiency of radial micropillar ZnO/ZnTe solar cell.

$1 \times 10^{19} \text{ cm}^{-3}$). As seen from Fig. 4.3, for a doping concentration of $1 \times 10^{18} \text{ cm}^{-3}$, the efficiency appears to be almost insensitive to the auger co-efficient (means auger recombination rate). On a different note, lower doping concentration leads to lower efficiency when the auger recombination co-efficient (means auger recombination rate) is low.

4.3 Optimized Doping Profile

The above discussion leads to the conclusion that a doping concentration of $2 \times 10^{19} \text{ cm}^{-3}$ is preferable. This matches well with the value reported in [83]. Rucksana Safa Sultana, Ali Newaz Bahar *et al* [83] reported $2 \times 10^{19} \text{ cm}^{-3}$ (p-type) acceptor doping density of ZnTe thin film; therefore, we intend to explore the effect of lower and higher doping concentration than $2 \times 10^{19} \text{ cm}^{-3}$ on the electrical performance of the device. The doping

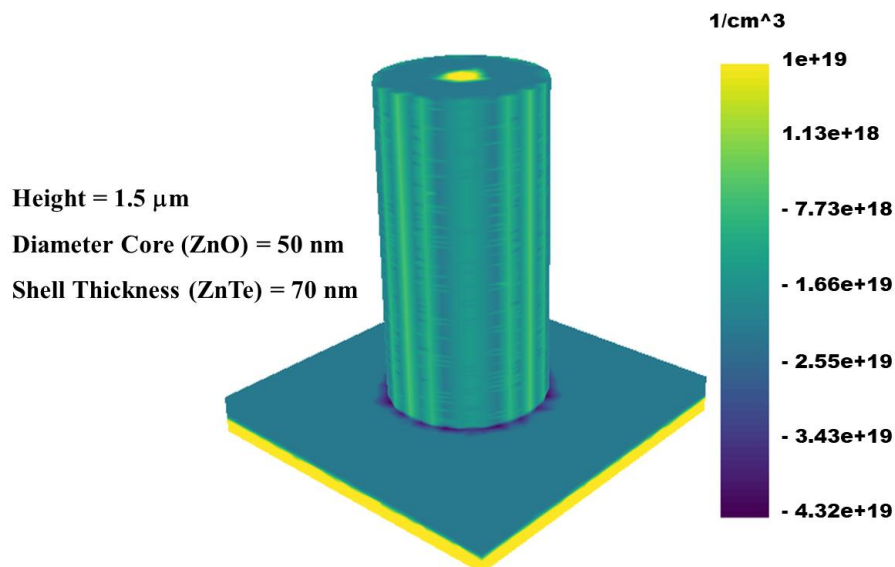


Figure 4.4: Doping profile for radial core-shell micropillar ZnO/ZnTe solar cell of 1.5 μm height.

concentration for the ZnO core has been chosen to be $1 \times 10^{19} \text{ cm}^{-3}$ as reported in [83]. The ZnO core, being a high bandgap material, is somewhat insensitive to auger recombination. Figure 4.4 illustrates the doping profile for the radial micropillar ZnO/ZnTe solar cell. This doping profile has been used for subsequent simulations.

4.4 Summary

Doping concentration in the range of 1×10^{18} to $3 \times 10^{19} \text{ cm}^{-3}$ (ZnTe layer) has been explored to observe the electrical performance of the device. The choice of doping concentration must balance between high enough carrier concentration that leads to high efficiency and lower enough recombination to result in maximum efficiency. Based on the analysis on auger recombination rate coupled with doping concentration, a doping concentration of $2 \times 10^{19} \text{ cm}^{-3}$ is chosen which has been reported in [84].

CHAPTER 5

PERFORMANCE ANALYSIS OF ZnO/ZnTe MICROPILLAR SOLAR CELL

This chapter analyzes the influence of the pillar height, pitch and diameter on electrical and optical characteristics of the radial ZnO/ZnTe micropillar solar cell. To understand the impact on device characteristics, each of these parameters has been varied individually keeping the others constant. That has ensured sensitivity to only the relevant parameters.

5.1 Effect of Pillar Length

Pillar length is an important parameter which needs to be optimized in order to obtain high efficiency in a pillar-based solar cell. Tuning the pillar height largely affects the optical and electrical performance of the device. The optical and electrical performance of the device have been discussed below in separate subsections.

5.1.1 Optical Analysis

As shown in Fig. 5.1 (a, b and c), increasing the pillar height significantly decreases the reflection and transmission of light and thus increases the absorption of light within the entire light spectrum (400 nm - 700 nm). A range of pillar height between 1.5 μm to 4 μm has been considered for the analysis. A report [85] on ZnO/CdTe core-shell nanowire has claimed to successfully fabricate (height, 1 μm) the nanowires using both chemical bath deposition and close space sublimation. Therefore, we intended to observe both optical and electrical performance of ZnO/ZnTe core-shell micropillar structure where the pillar height

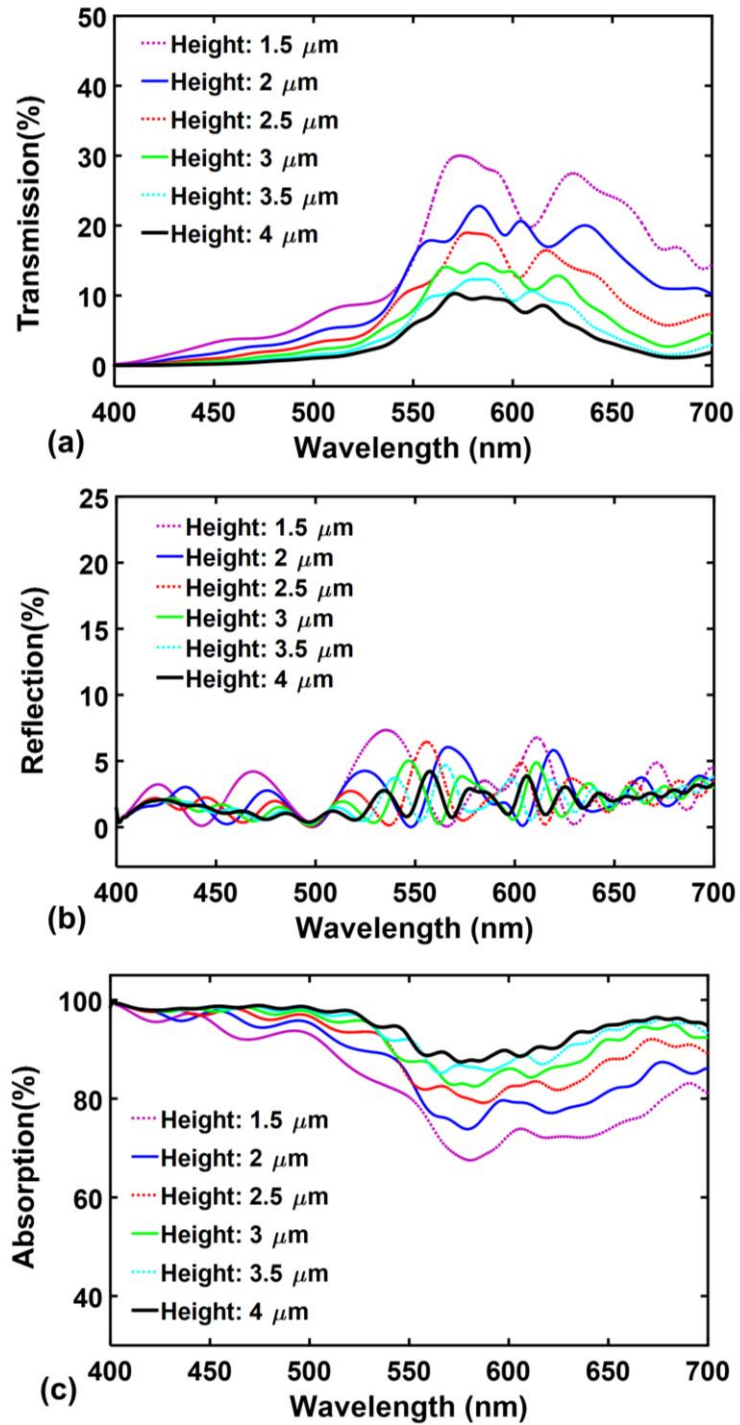


Figure 5.1: Effect of pillar-height on (a) transmission (b) reflection and (c) absorption percentage of a radial micropillar ZnO/ZnTe solar cell.

is longer than 1.5 μm . The scenario explains that longest pillar height will provide the best

optical performance. A height of 4 μm pillar leads to least amount of reflection (Fig. 5.1 (b), marked in black) and highest absorption (Fig. 5.1 (c), marked in black). On the other hand, the lowest height (1.5 μm) provides highest reflection and lowest absorption. The minimum pillar height (**1.5 μm**) cannot trap significant portion of incident light within the pillar-structure. For this case, most of the light bounces back and causes higher reflection and transmission. Apparently, the absorption increases (therefore-reflection and transmission decreases) proportionally with the pillar height. Increasing the pillar height improves the light trapping ability. However, longer pillar height ($> 4 \mu\text{m}$) leads to complexity in the simulation (FDTD solver). It requires more memory space to run the file which results in huge simulation time. Therefore, we decided to run the simulation in FDTD at a start point of 1.5 μm height and stop at a height of 4 μm .

5.1.2 Electrical Analysis

The optical analysis of the device alone does not provide the complete scenario. Electrical analysis is essential in order to understand the device physics of the solar cell. Electrical analysis calculates the collection of the carriers which determines the output power of a solar cell. Diffusion length of the generated carriers, recombination and defect states in the material are some of the essential factors that are taken into consideration while analyzing electrical performance of the device. These factors play very important roles to determine the collection of the carriers. The electrical performance parameters (V_{oc} , J_{sc} , FF and efficiency) of the core-shell ZnO/ZnTe micropillar solar cell are shown in Fig. 5.2 (a - d) as functions of the vertically aligned pillar height. Current density and efficiency both

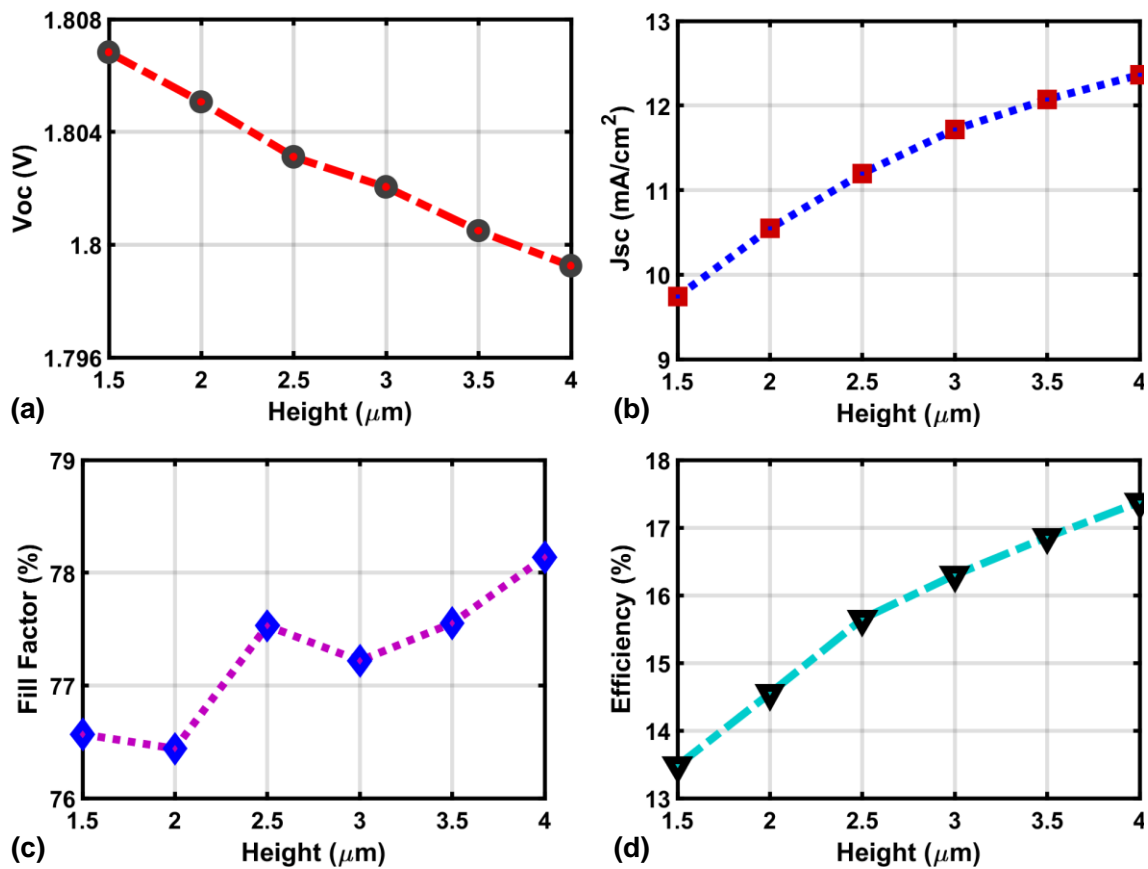


Figure 5.2: Effect of pillar-height on (a) V_{oc} (b) J_{sc} (c) fill factor and (d) efficiency of a radial micropillar ZnO/ZnTe solar cell.

increase with the pillar height. The reason is that the absorption of light increases with the increase of the pillar height. Note that most of the electron-hole pairs in a core-shell ZnO/ZnTe micropillar solar cell are generated in the ZnTe shell. The collection of carriers and absorption of light is orthogonal. That is the main reason why increase of pillar height does not hinder in the collection of carriers. Therefore, the short circuit current density and efficiency increases with the pillar height (shown in Fig. 5.2 (b, d)). For a height of 4 μm, the J_{sc} and efficiency is 12.36 mA/cm² and 17.38 % respectively. On the other hand, increase in the pillar height leads to lower open circuit voltage (V_{oc}). However, the degree

of reduction is extremely small. The variation of the light illumination in the upper and lower portion of the pillars leads to overall reduction in the V_{oc} of the device. Fig. 5.2 (a) exhibits that at 1.5 μm and 4 μm of pillar height, the value of V_{oc} is 1.806 V and 1.799 V respectively. The V_{oc} can be obtained using the equation (2.1) where the change in V_{oc} logarithmically depends on the excess carrier concentration. The change in V_{oc} in Fig 5.2 (a) clearly follows equation (2.1). From the I-V characteristic curve of Fig. 5.3 (a), we can easily understand that the open circuit voltage (V_{oc}) for all of the cases remain the same, but the short circuit current density increases with the increase of the pillar height. For a height of 4 μm , we observe the best I-V performance (marked in black in Fig. 5.3 (a)). Similarly, the power curve depicted in Fig. 5.3 (b) indicates that 4 μm pillar height ensures the highest output power (marked in black in Fig. 5.3 (b)). On the other hand, the output power curve is lowest for the pillar height of 1.5 μm . Therefore, as per electrical analysis, 4 μm pillar height provides the best performance for ZnO/ZnTe micropillar solar cell while exploring the pillar height between 1.5 μm to 4 μm .

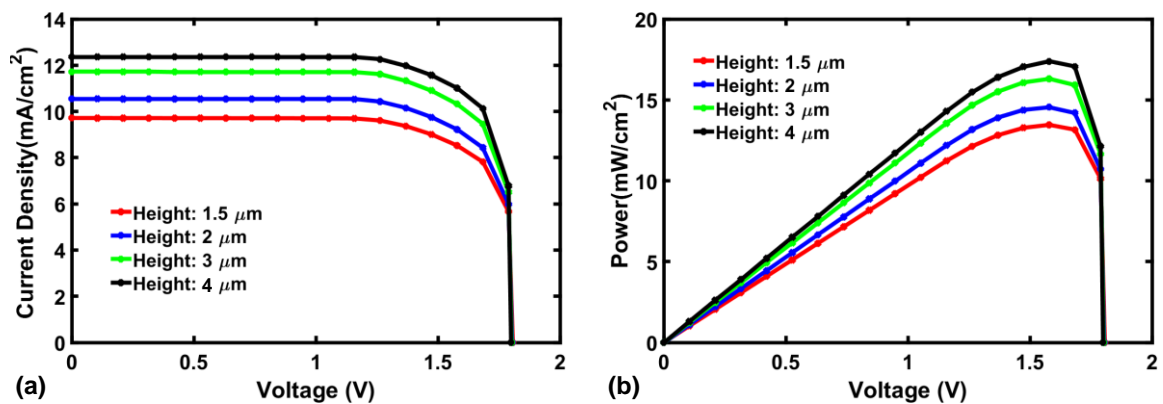


Figure 5.3: Effect of pillar-height on (a) current density and (b) power density of a radial micropillar ZnO/ZnTe solar cell.

5.1.3 Summary

Considering both the optical and electrical responses, we conclude that increasing the pillar height leads to better performance of the device. Minority carrier lifetime and high absorption of the material are the two main factors determining the energy-conversion-efficiency [76]. Orthogonal direction between light absorption and carrier collection makes the micropillar core-shell structure unique [86]. Even materials with short minority carrier diffusion length could be used in this structure, thereby reducing the cost of materials. Therefore, this core-shell micropillar promises higher collection of carriers while reducing the material cost. The height of the pillar can be as long as needed to absorb maximum incident light without hindering the collection of the carriers due to the unique structure of the device. As discussed in section 2.4.2, CdTe requires 5~10 μm of thickness to ensure maximum light absorption. Like CdTe, ZnTe (II-VI) material is considered to have a high absorption coefficient. Therefore, increasing the height of the pillar to a level of 10 μm may lead to the best optimum efficiency for the core-shell ZnO/ZnTe micropillar solar cell. Due to the limitation of the FDTD solver, increasing the pillar height ($> 4 \mu\text{m}$) raises the computational complexity, both in memory space and in simulation time. Therefore, the exploration of the pillar height has been stopped at 4 μm pillar height. In summary, increasing the height of the ZnO/ZnTe core-shell micropillar solar cell causes higher absorption and thus increases J_{sc} and efficiency. Note that the pitch and diameter of the micropillars have been kept constant at 0.4 μm and 190 nm respectively. These variables will be explored in the next two sections.

5.2 Effect of Pitch

Another important geometry factor to optimize is the pitch of the pillars. Pitch (P) represents the geometric separation between two adjacent pillars. It is possible that one particular pitch value might provide good optical performance but not necessarily good electrical performance. The effect of pitch on the optical and electrical performance of the ZnO/ZnTe core-shell micropillar solar cell has been discussed below.

5.2.1 Optical Analysis

Pitch determines the interaction of light within the device. The light trapping ability of the device largely depends on the pitch value. Figure 5.4 (a - c) represents absorption, reflection and transmission of the ZnO/ZnTe micropillar solar cell as a function of distance between two nearby pillars. To continue with the pitch exploration, the height of the pillar is set to 4 μm and the diameter of the pillar is fixed to 190 nm. It is clear from the analysis that the relation between the pitch variable and output optical response is not proportional in nature. Minimum pitch value of 0.2 μm and maximum pitch value of 0.6 μm (colored in black and pink respectively) leads to the worst optical performance of the device. The starting point of the pitch value is 0.2 μm for our further research because there has been a report on the Si NW where the minimum starting pitch value was 0.2 μm [87]. For that reason, we chose to investigate the behavior of the device (ZnO/ZnTe core-shell micropillar) while increasing the pitch value ($> 0.2 \mu\text{m}$). At minimum 0.2 μm pitch value, the pillars are very close to each other which results in higher light reflection shown in Fig.

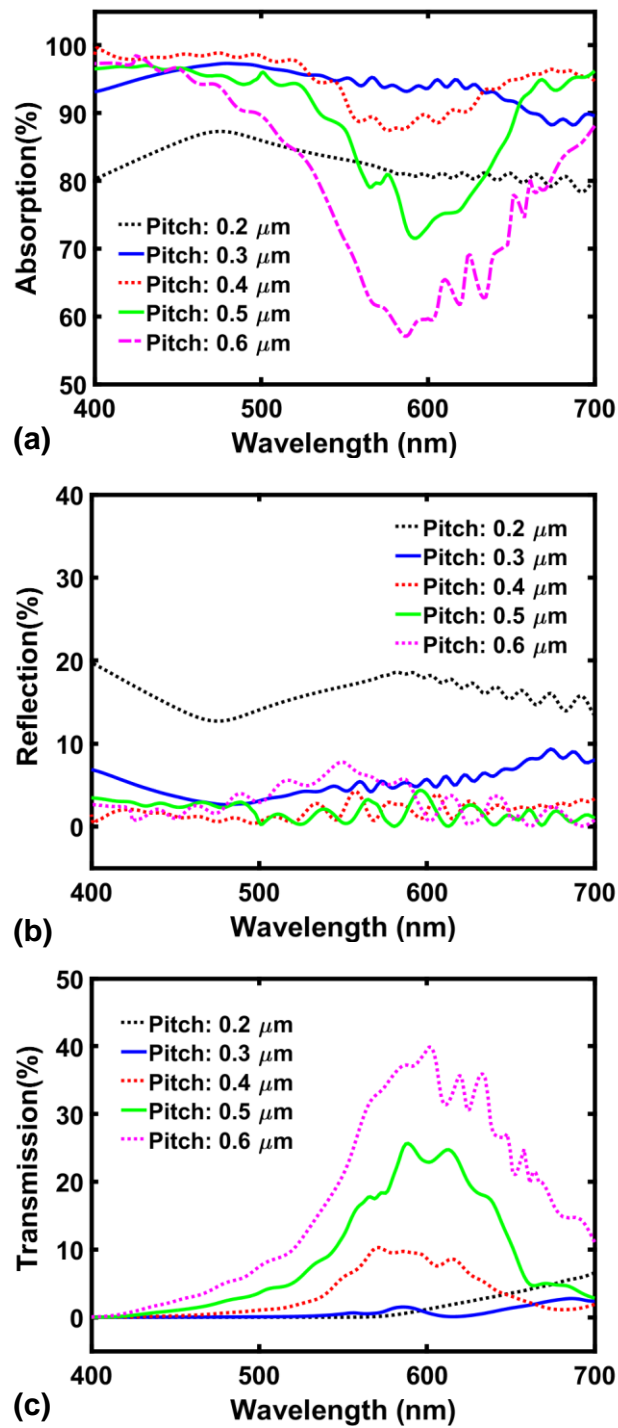


Figure 5.4: Effect of pitch of the pillars on (a) transmission (b) reflection and (c) absorption percentage of a radial micropillar ZnO/ZnTe solar cell.

5.4 (b). Most of the incident light bounces off from the top surface rather than getting

trapped within two nearby pillars. Therefore, lower absorption of light occurs over the entire wavelength range (400 nm – 700 nm), as depicted in Fig. 5.4 (a). On the other hand, the maximum pitch value of 0.6 μm (colored in pink), allows maximum light transmission (Fig 5.4 (c)) and results in low light reflection (Fig. 5.4 (b)). Thus, light absorption drastically decreases due to higher light transmission at 0.6 μm pitch value. As a result, too low ($< 0.3 \mu\text{m}$) and too high ($> 0.5 \mu\text{m}$) pitch values are not suitable for optimum performance. However, 0.3 μm , 0.4 μm and 0.5 μm pitch values provide the best optical performance. Among the three of these choices, a 0.3 μm pitch value provides better absorption, reflection and transmission as shown in Fig. 5.4 (a - c) (marked in blue color). Though 0.4 μm distance between two pillars ensures lower reflection, it leads to higher transmission over a certain wavelength region (500 nm - 650 nm). Therefore, a lower absorption of light occurs within a region of 550 nm to 620 nm as shown in Fig. 5.4 (a). In addition to that, as shown in Fig. 5.4 (a - c), 0.5 μm pitch value certainly offers lower reflection over the entire region but leads to higher transmission than 0.3 μm and 0.4 μm pitch values. As a result, it causes lower absorption of light as shown in Fig. 5.4 (a) in green color. As mentioned before, it is important to consider the electrical performance together with the optical responses to determine the devices' overall performance. We discuss the electrical performance in the next section.

5.2.2 Electrical Analysis

Fig. 5.5 (a - d) presents the electrical performance parameters (V_{oc} , J_{sc} , FF and efficiency) with the variation of pitch (P). There is no linear relation between pitch value and the

efficiency of the core-shell ZnO/ZnTe micropillar solar cell which can be easily concluded from Fig. 5.5 (d). During the electrical analysis, the height and total diameter of the pillar are kept at 4 μm and 190 nm respectively. Considering Fig. 5.5 (a), the open circuit voltage (V_{OC}) increases linearly but the change is very minor to be considered. At minimum 0.2 μm and maximum 0.6 μm pitch values, the V_{OC} is increased from 1.78 V to 1.80 V. This

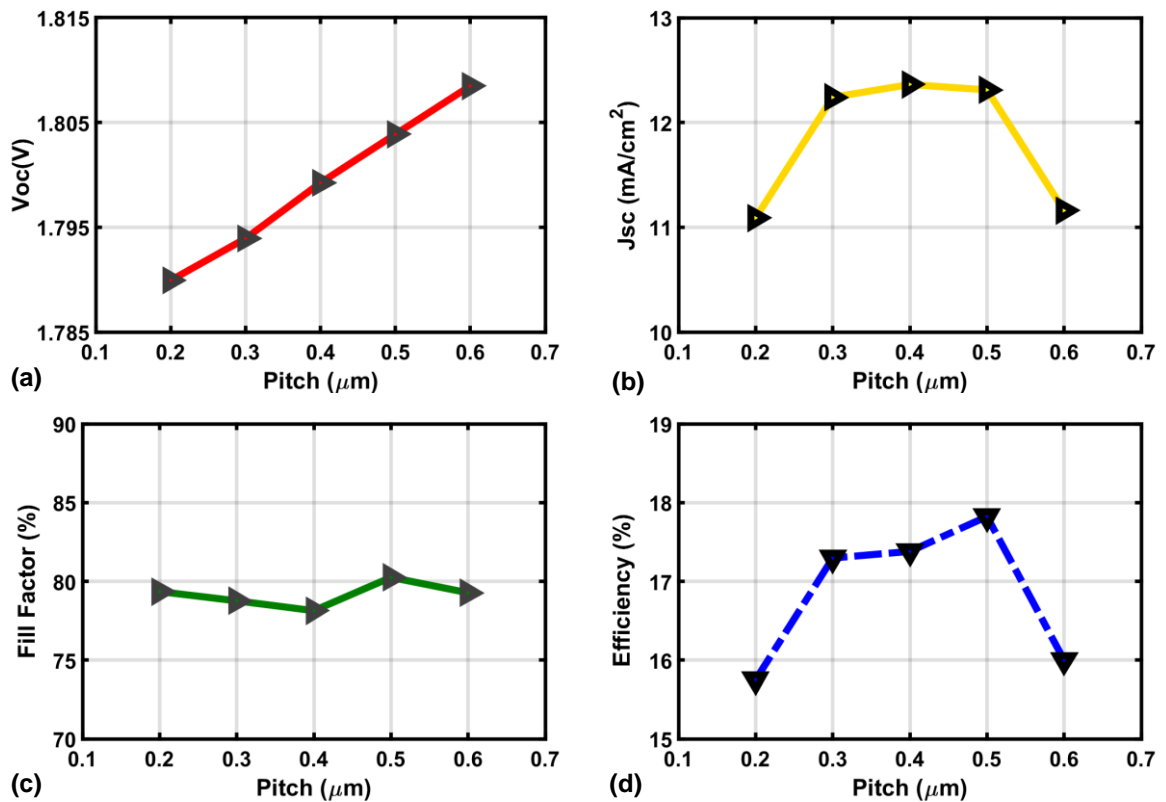


Figure 5.5: Effect of pitch of the pillars on (a) V_{OC} (b) J_{SC} (c) fill factor and (d) efficiency of a radial micropillar ZnO/ZnTe solar cell.

minor change V_{OC} can also be seen in Fig. 5.6 (a, b). However, minimum 0.2 μm and maximum 0.6 μm pitch values offer lower efficiency and short circuit current density (J_{SC}).

Clearly, the worst performance in terms of electrical characteristics occur at 0.2 μm and 0.6 μm pitch values. The worst responses for optical characteristics were also observed for these two pitch values. Lower light absorption results in lower carrier generation and thereby leads to lower short circuit current density (J_{SC}) and efficiency. On the other hand,

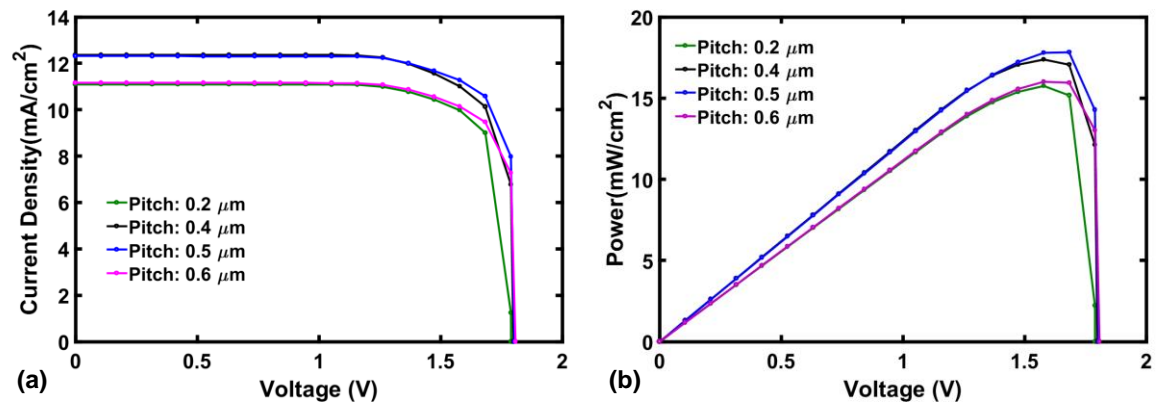


Figure 5.6: Effect of pitch of the pillars on (a) current density and (b) power density of a radial micropillar ZnO/ZnTe solar cell.

the other three choices (0.3 μm , 0.4 μm and 0.5 μm) provide almost similar J_{SC} as shown in Fig. 5.5 (b). But, Fig. 5.5 (d) shows the best efficiency of 17.82 % at 0.5 μm pitch value. At 0.3 μm and 0.4 μm , the efficiency is 17.29 % and 17.38 %, respectively. Even the fill factor is maximum at 0.5 μm pitch value, as shown in Fig. 5.5 (c). On the other hand, Fig. 5.6 (a, b) depicts the I-V characteristic curve and power density curve of the ZnO/ZnTe micropillar solar cell with different pitch values. I-V characteristic plots (Fig. 5.6 (a)) demonstrate that both 0.2 μm and 0.6 μm pitch values generate equally degraded characteristics. But, 0.4 μm and 0.5 μm pitch values show similar improvements in the I-

V characteristic. Also, the power curve shows better output power for 0.5 μm pitch value (Fig. 5.6 (b)).

5.2.3 Summary

Considering both the optical and electrical characteristics of the ZnO/ZnTe micropillar solar cell, low (0.2 μm) and high (0.6 μm) pitch values have proven to be sub-optimal. Both of these pitch values yield lower efficiency and lower J_{SC} . As for the intermediate values of pitch (0.3 μm , 0.5 μm and 0.6 μm), electrical analysis shows best performance for 0.5 μm . On the other hand, optical analysis shows best response at 0.3 μm . To ensure balance between optical and electrical characteristics and ensure eventual performance benefits, 0.5 μm has been chosen as the optimum value of the pitch.

5.3 Effect of Pillar Diameter

Pillar diameter is another important parameter which affects the efficiency of the solar cell. ZnO, a wide bandgap (3.3 eV) material, forms the core, and ZnTe forms the shell in this core-shell structure. As shown in Fig. 3.13 (d), most of the light absorption and carrier generation have happened in the outer (ZnTe) shell of the device. Therefore, changing the diameter of ZnO will have little effect on generating carriers and therefore will not affect the output power. As a result, only the outer (ZnTe) shell thickness should be varied for further exploration of the device. The optical and electrical analysis of the ZnO/ZnTe micropillar solar cell has been described in the following two subsections with the variation of the outer (ZnTe) shell thickness from 70 nm to 130 nm.

5.3.1 Optical Analysis

The diameter of the ZnO has been kept fixed at 50 nm for our further analysis. During the analysis of the ZnO/CdTe core-shell micropillar solar cell reported in a paper [85], the ZnO core has been chosen to be 50 nm in diameter and the shell thickness (CdTe) has been varied from 50 nm to 100 nm. Therefore, we decided to explore the device performance of the ZnO/ZnTe core-shell micropillar solar cell with shell thickness (ZnTe) variation between 50 nm and 130 nm. The optical analysis of the ZnO/ZnTe micropillar solar cell promises lower reflection and higher absorption over the wavelength regime of 400 nm to 500 nm while changing the thickness of the ZnTe shell (shown in Fig. 5.7). However, the absorption increases in the wavelength regime of (500 nm - 620 nm) when the shell thickness is 130 nm (green curve). Maximum shell thickness of 130 nm reflects maximum light, while minimum light is reflected with shell thickness of 70 nm as shown in Fig. 5.7 (b). However, electrical analysis must be done for the overall assessment of the solar cell performance. During the shell thickness exploration, pillar height and pitch were kept fixed at 4 μm and 0.5 μm values.

5.3.2 Electrical Analysis

Fig. 5.8 (a - d) shows the electrical performance of the radial ZnO/ZnTe micropillar solar cell with various diameters. As reported in [88], higher efficiency of the silicon pillar array

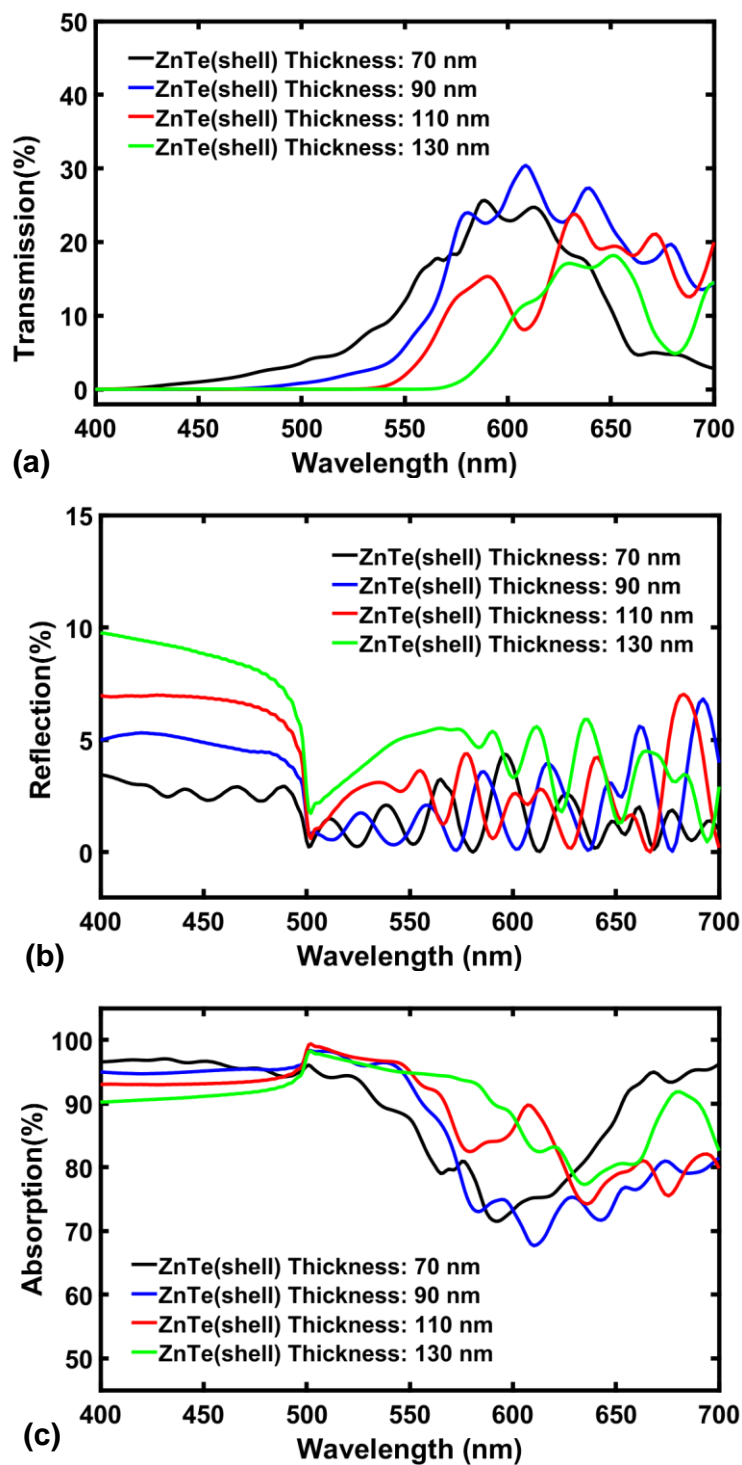


Figure 5.7: Effect of diameter of pillars on (a) transmission (b) reflection and (c) absorption percentage of a radial micropillar ZnO/ZnTe solar cell.

solar cell is linked to higher J_{SC} which is caused by higher absorption thickness and short

minority carrier length. Increasing the shell thickness ensures more absorption of light and therefore higher carrier generation. The separation of these generated carriers is orthogonal to the incident light. Therefore, the radial p-n junction plays a significant role in the collection of these carriers. If the thick outer (ZnTe) shell hinders in the collection of the carriers, then there is no additional advantage of this pillar architectural design compared to the planar structure. Generated carriers in the shell (ZnTe) will not get collected by the p-n junction if the minority carrier diffusion length is smaller than the thickness of the shell. Short circuit current density (J_{SC}), fill factor (FF), and efficiency decreases as the shell

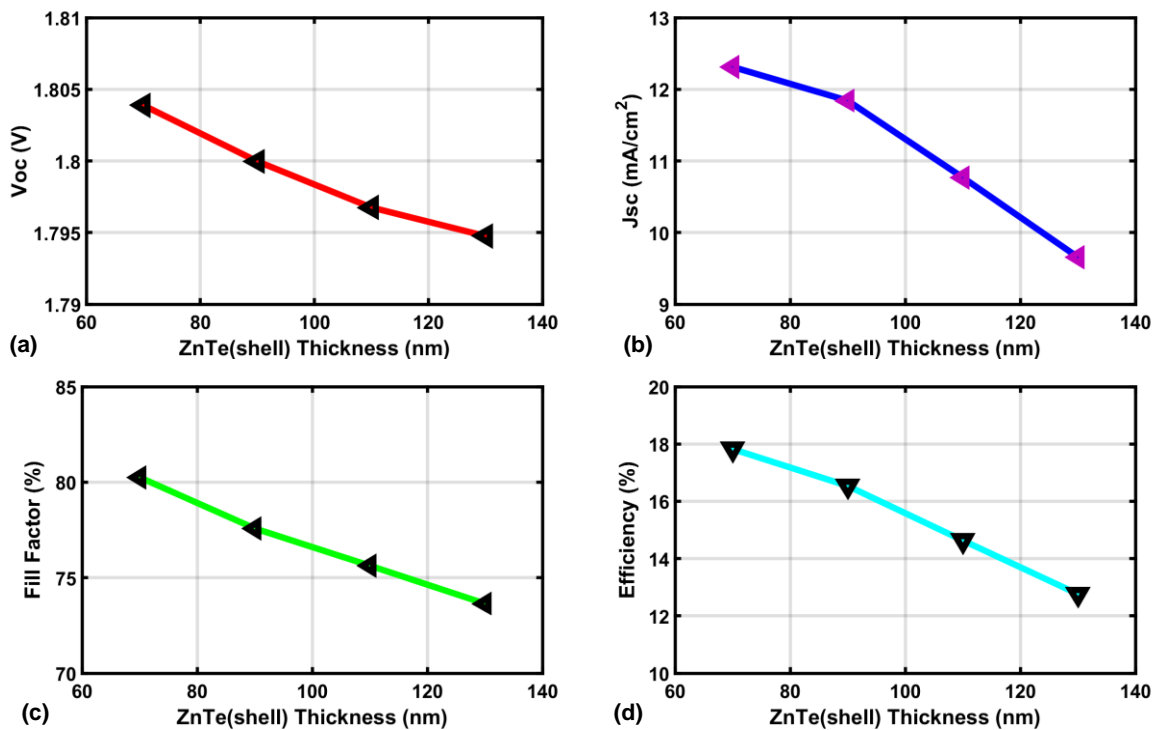


Figure 5.8: Effect of diameter of the pillars on (a) V_{OC} (b) J_{SC} (c) fill factor and (d) efficiency of a radial micropillar ZnO/ZnTe solar cell.

thickness increases. This phenomenon has been demonstrated in Fig. 5.8 (b - d). Thus, generated carriers with smaller diffusion length in the shell (ZnTe) cannot reach the radial p-n junction for larger shell thickness (130 nm). Most of the generated carriers get recombined within the shell before getting collected by the p-n junction. Thus, J_{SC} and efficiency decreases. Open circuit voltage (V_{OC}) also decreases with increasing shell thickness. As the change in V_{OC} occurs logarithmically, the change is barely noticeable

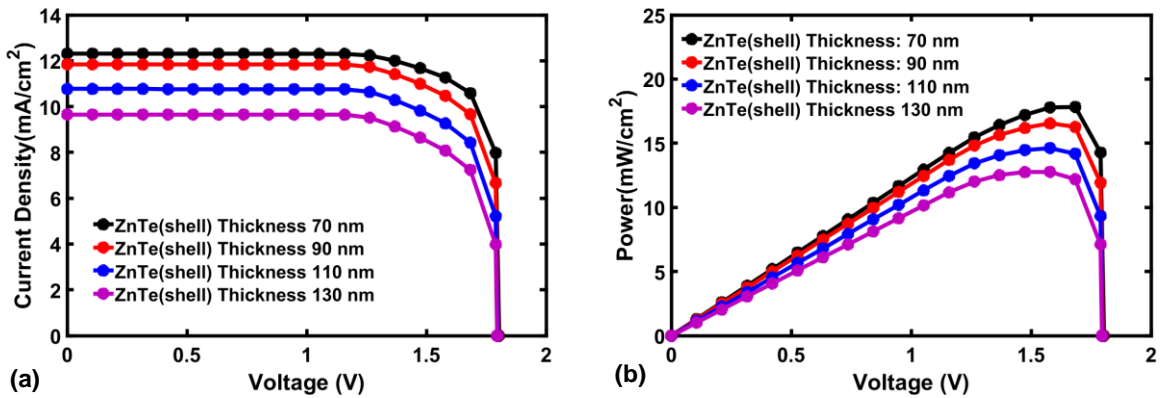


Figure 5.9: Effect of diameter of the pillars on (a) current density and (b) power density of a radial micropillar ZnO/ZnTe solar cell.

(Fig. 5.8 (a)). Increasing the diameter of the pillar increases the surface area and thereby increases the rate of surface recombination. This is also a major factor that needs to be considered while designing a solar cell device. Figure 5.9 (a, b) shows that increasing the diameter of the pillars reduces the short circuit current density and the output power. The black curve in Fig. 5.9 (a) shows the I-V characteristic curve of the ZnO/ZnTe radial junction micropillar solar cell with highest short circuit current density (J_{SC}). The J_{SC} and efficiency of the ZnO/ZnTe micropillar solar cell at minimum shell thickness of 70 nm are

12.31 mA/cm² and 17.82 % respectively. This electrical analysis has been carried out while the height of the pillar and the pitch are kept fixed at 4 μm and 0.5 μm respectively.

5.3.3 Summary

Higher shell thickness (hence larger pillar diameter) leads to better absorption efficiency and a larger number of photo generated carriers. In that regard, larger shell thickness (hence large diameter) appears to be favorable for improved solar cell performance (as per optical simulation). However, minority carrier diffusion length sets an upper limit to the allowable thickness of the shell. If the thickness exceeds the diffusion length of the minority carriers, recombination becomes a concern and overall efficiency suffers. However, thinning the shell thickness will lead to lower generation of carriers. Thinner shell thickness (< 50 nm of ZnTe) eventually causes the computational file to run almost 2 hours to obtain the outcome from the FDTD solver. On the other hand, the simulation diverges while utilizing the DEVICE solver. This is because the certain p-n junction area (depletion region) at the interface of the core-shell will be heavily affected in the presence of very thin shell thickness. In addition, complexity arises while fabricating a very thin layer on top of the core layer. It requires a very sophisticated process which increases the manufacturing cost.

CHAPTER 6

FUTURE WORK AND CONCLUSION

This chapter discusses some potential future extensions to the contributions presented throughout the previous chapters. It also summarizes and concludes the entire thesis.

6.1 Possible Future Extensions

As the interest on micropillar solar cell is growing with time, there could be several possible extensions to the contributions of this work. Proposed extensions and future work are briefly discussed below.

6.1.1 Analysis of ZnO/ZnTe Solar Cells with Triangular Surface Geometry

As a variant of the pillar-type structure which is cylindrical in geometry, other forms of micropillars (triangular/cone/dome type) have also been proposed in the literature [75]. These structures have their own advantages and challenges. An analysis similar to the ones presented in this work will be of great interest to the solar cell research community. However, extensive modifications will be required in the simulator to capture the geometric variants. It will be necessary to choose and set appropriate boundary conditions based on the pillar geometry.

6.1.2 Analyzing the Effect of Radiative and Shockley-Read-Hall Recombination

In addition to the auger recombination, it is possible to observe radiative and shockley-read-hall recombination in ZnO/ZnTe solar cell structures. An interesting future project would be to explore the severity and implications of these phenomena in determining the solar cell performance. A comparison can be made between different solar-cell configurations to identify the relative influence of these variants. Innovative geometry and material combinations can be explored to minimize all of these forms of recombination.

6.1.3 Exploring the Effect of Different Metal Contacts

Metal contacts play an important role in determining the collection efficiency in a solar cell. As for micropillar structures, there are several options for depositing the metal layers as contacts, including Laser Metal Deposition (LMD) and Thermal Vapor Deposition. Transparency and conductivity of the metals can be expected to have major implications on the overall efficiency. Further analysis can be done to explore the effect of such metal layers (with different material and geometry) on the performance of the solar cell.

6.2 Conclusion

ZnO/ZnTe-based solar cells hold immense promise for commercialization in the near future. This work presented a comprehensive analysis and comparison between different versions of ZnO/ZnTe-based solar cells. Comparison between planar and micropillar structures of the ZnO/ZnTe-based solar cell reveal clear benefits of micropillar structures.

Further analysis shows that radial micropillars offer better optical and electrical performance compared with the axial variant. We showed that the ideal J_{SC} for the radial micropillar ZnO/ZnTe solar cell has reached up to 24.47 mA/cm² with a maximum generation rate of $4.27 \times 10^{28} \text{ m}^{-3}\text{s}^{-1}$. Analysis of the impact of variations in the doping profile led to the choice of $2.16 \times 10^{19} \text{ cm}^{-3}$ as the optimum doping concentration for the ZnTe shell, considering the coupled effect of auger recombination rate and doping density. Investigation of pillar parameters showed that a pillar height of 4 μm had the highest level of absorption and lowest level of reflection while exploring in the range of 1.5 μm to 4 μm height. The optimum pitch has been chosen to be 0.5 μm considering the trade-off between optical and electrical responses. Finally, a pillar diameter of 190 nm (with shell thickness of 70 nm) has showed minimum carrier recombination and lower material cost.

CHAPTER 7

REFERENCES

- [1] A. Williams, "Role of fossil fuels in electricity generation and their environmental impact," in *IEE Proceedings A - Science, Measurement and Technology*, vol. 140, no. 1, pp. 8-12, Jan. 1993.
- [2] M. A. Usova and V. I. Velkin, "Possibility to use renewable energy sources for increasing the reliability of the responsible energy consumers on the enterprise," *2018 17th International Ural Conference on AC Electric Drives (ACED)*, Ekaterinburg, 2018, pp. 1-4.
- [3] (2019), *World Total Primary Energy Consumption, 2015*, [Online]. Available : [https://commons.wikimedia.org/wiki/File:World_Total_Primary_Energy_Consumption_by_Fuel_\(2015\).svg](https://commons.wikimedia.org/wiki/File:World_Total_Primary_Energy_Consumption_by_Fuel_(2015).svg)
- [4] (2019), *U.S. Energy Consumption by Energy Source, 2016*, [Online]. Available: <https://alternativeenergy.procon.org/view.additional-resource.php?resourceID=006776>
- [5] (2019), *Best Research Cell Efficiency Chart, 2019*, [Online]. Available: <https://www.nrel.gov/pv/cell-efficiency.html>
- [6] Orthi Sikder, Camille Torres and Peter Mark Jansson, "Comparative Analysis of Enerfy Storage for Photovoltaics:Electrical vs Virtual," *ASES National Solar Conference 2018*. DOI: 10.18086/solar.2018.01.11
- [7] (2019), *Solar PV Capacity and the System Price*, [Online]. Available: https://en.wikipedia.org/wiki/Growth_of_photovoltaics.
- [8] (2019), *Solar Industry Research Data*, [Online]. Available: <https://www.seia.org/solar-industry-research-data>.
- [9] S. Taggart, G. James, Z. Dong and C. Russell, "The Future of Renewables Linked by a Transnational Asian Grid," in *Proceedings of the IEEE*, vol. 100, no. 2, pp. 348-359, Feb. 2012.
- [10] (2019), *Typical Solar Cell Mechanism*, [Online]. Available: <https://www.engineering.com/SustainableEngineering/RenewableEnergyEngineering/SolarEnergyEngineering/Photovoltaics/tabid/3890/Default.aspx>.

- [11] (2019), *Band Diagram of the Typical Solar Cell*, [Online]. Available: https://en.wikipedia.org/wiki/Theory_of_solar_cells.
- [12] J.D.Murphy, R.E.McGuire K.Bothe *et al*, “Minority carrier lifetime in silicon photovoltaics: The effect of oxygen precipitation”, in *Solar Energy Materials and Solar Cells*, vol.120, pp. 402-411, 2013.
- [13] M.R.I.Ramadan *et al*, “Effect of minority carrier lifetime in solar cells”, in *Solar and Wind Technology*, vol. 6, pp. 615-618, Feb 2003.
- [14] Purnomo Sidi Priambodo *et al*, “Electric Energy Engineering and Management in Solar Cell System”, in *INTECH Open Science*, 2013.
- [15] Bert Stegemanna, Jan Kegela, Erhard Conradb *et al*, “Evolution of the charge carrier lifetime characteristics in crystalline silicon wafers during processing of heterojunction solar cells”, in *4th International Conference on Silicon Photovoltaics*, pp. 219-228, 2014.
- [16] Dr S S Verma, “Next Generation Solar Cell”, 2016.
- [17] K. R. Catchpole and M. A. Green, "Third generation photovoltaics," *2002 Conference on Optoelectronic and Microelectronic Materials and Devices. COMMAD 2002. Proceedings (Cat. No.02EX601)*, Sydney, NSW, Australia, 2002, pp. 59-64.
- [18] Dong Rip Kim, Chi Hwan Lee *et al*, "Hybrid Si Microwire and Planar Solar Cells: Passivation and Characterization", in *Journal of American Chemical Society*, 2011.
- [19] Brendan M. Kayes *et al*, "Comparison of the device physics principles of planar and radial p-n junction nanorod solar cells", in *Journal of Applied Physics*, vol. 97, 2005.
- [20] Yang Zeng, Qinghao Ye and Wenzhong Shen *et al* “Design principles for single standing nanowire solar cells: going beyond the planar efficiency limits”, in *Scientific Reports*, May 2014.
- [21] C.K. Huang, K.W. Sun and W.-L. Chang *et al*, “Efficiency enhancement of silicon solar cells using a nano-scale honeycomb broadband antireflection structure”, in *Optical Society of America*, 2011.
- [22] (2018), “*Basic Photovoltaic Principles and Methods*”, [Online], Available : <http://energy-models.com/basic-photovoltaic-principles-and-methods>.

- [23] Majid Gharghi, Ehsanollah Fathi and Boubacar Kante *et al*, "Heterojunction Silicon Microwire Solar Cells", in *NANO LETTERS*, vol. 12, pp. 6278-6282, 2012.
- [24] Neil P. Dasgupta¹, Peidong Yang *et al*, "Semiconductor nanowires for photovoltaic and photoelectrochemical energy conversion", in *Review Article*, 2013.
- [25] Dang, Hongmei, "Nanostructured Semiconductor Device Design in Solar Cells" (2015). *Theses and Dissertations--Electrical and Computer Engineering*. 77.
- [26] Prachi Patel *et al*, "Nanopillar Solar Cells", *MIT Technology Review*, 2009.
- [27] Joshua Schrier *et al*, " Optical Properties of ZnO/ZnS and ZnO/ZnTe Heterostructures for Photovoltaic Applications," in *American Chemical Society*, 2007.
- [28] Songping Luo, Xiaoli He, *et al*, "Vertically aligned ZnO/ZnTe core/shell heterostructures on an AZO substrate for improved photovoltaic performance", in *RSC Advances*, 2017.
- [29] J.C.Fan, K.M.Sreekanth, Z.Xie *et al*, "p-Type ZnO materials: Theory, growth, properties and devices", in *Progress in Material Science*, 2013.
- [30] Liang Li, Tianyou Zhai and Yoshio Bando, "Recent progress of one-dimensional ZnO nanostructured solar cells", in *Nano Energy*, 2012.
- [31] Kewei Liu, Makoto Sakurai and Masakazu Aono *et al*, "ZnO-Based Ultraviolet Photodetectors", in *NCBI*, 2010.
- [32] Joshua Schrier, Denis O. Demchenko and Lin-Wang *et al*, "Optical Properties of ZnO/ZnS and ZnO/ZnTe Heterostructures for Photovoltaic Applications", in *NANO Letters*, 2007.
- [33] W. Wang, Albert Lin *et al*, "Electrical Characteristics and Photoresponse of ZnO/ZnTe Heterojunction Diodes", in *Electronic Materials*, 2008.
- [34] YuWei Lin, Wei-Jen Chen, Jiun You Lu, Yuan Huei Chang *et al*, "Growth and characterization of ZnO/ZnTe core/shell nanowire arrays on transparent conducting oxide glass substrates", in *Nanoscale Research Letter*, 2012.
- [35] M.Sookhakian *et al*, "Synthesis, structural, and optical properties of type-II ZnO–ZnS core–shell nanostructure", in *Journal of Luminence*, vol. 145, pp- 244-252, 2014.

- [36] YuWei Lin *et al*, "Growth and characterization of ZnO/ZnTe core/shell nanowire arrays on transparent conducting oxide glass substrates", in *Nanoscale Research Letters*, 2012.
- [37] Yiyao Cao, Zhiming Wu *et al*, "Type-II Core/Shell Nanowire Heterostructures and Their Photovoltaic Applications," in *Nano-Micro Letters*, vol. 4, pp 135–141, 2012.
- [38] PenghuiGuo *et al*, "ZnS/ZnO heterojunction as photoelectrode: Type II band alignment towards enhanced photoelectrochemical performance," in *International Journal of Hydrogen Energy*, vol. 38, pages 13097-13103, 2013.
- [39] Giacomo Mariani *et al*, "High-efficiency nanopillar solar cells employing wide-bandgap surface recombination barriers," in *The International Society for Optics and Photonics*, 2014.
- [40] Zhiyong Fan *et al*, "Challenges and prospects of nanopillar-based solar cells," in *Nano Research*, vol. 2, pp: 829, 2009.
- [41] Soichi Ito and Masayoshi Nakano, " Theoretical Molecular Design of Heteroacenes for Singlet Fission: Tuning the Diradical Character by Modifying π -Conjugation Length and Aromaticity," *2014 American Chemical Society*, 2015. Doi: <https://doi.org/10.1021/jp5103737>
- [42] M. Rathi *et al.*, "Thin film III–V photovoltaics using single-cry stalline-like, flexible substrates," *2015 IEEE 42nd Photovoltaic Specialist Conference (PVSC)*, New Orleans, LA, 2015, pp. 1-3. doi: 10.1109/PVSC.2015.7356232
- [43] D. Shahrjerdi, S. W. Bedell, C. Bayram and D. Sadana, "Flexible InGaP/(In)GaAs tandem solar cells with very high specific power," *2013 IEEE 39th Photovoltaic Specialists Conference (PVSC)*, Tampa, FL, 2013, pp. 2805-2808. doi: 10.1109/PVSC.2013.6745055
- [44] Makoto Konagi, Mitunori Sugimoto and Kiyoshi Takahashi, "High efficiency GaAs thin film solar cells by peeled film technology", in *Journal of Crystal Growth*, Vol. 45, pp- 277-280, 2002.
- [45] Tanaka A, Hirata M, Omura M *et al*, " Comparative study of the toxic effects of gallium arsenide, indium arsenide and arsenic trioxide following intratracheal instillations to the lung of Syrian golden hamsters.", 2000.
- [46] Andrew Blakers, Ngwe Zin, Keith R. McIntosh and Kean Fong *et al*, "High Efficiency Silicon Solar Cells", in *Energy Procedia*, vol.33, pp. 1-10, 2013.

- [47] E. M. Gaddy, "Cost performance of multi-junction, gallium arsenide, and silicon solar cells on spacecraft," *Conference Record of the Twenty Fifth IEEE Photovoltaic Specialists Conference - 1996*, Washington, DC, USA, 1996, pp. 293-296. doi: 10.1109/PVSC.1996.564003
- [48] Green, Martin A., "Third Generation Photovoltaics: Advanced Solar Energy Conversion", in *Springer*, p. 65, 2003.
- [49] Jesus Rangel-Cardenas and Hugo Sobral, "Optical Absorption Enhancement in CdTe Thin Films by Microstructuring of the Silicon Substrate", in *Materials (Basel)*, 2017. doi: 10.3390/ma10060607
- [50] (2019), Cadmium Telluride Solar Cells, [Online]. Available: <https://www.nrel.gov/pv/cadmium-telluride-solar-cells.html>.
- [51] P. Vorobiyenko, I. Dmitrieva and A. Solomko, "Analytic solutions and numerical implementation of the specific electromagnetic wave propagation," *2016 IEEE International Conference on Mathematical Methods in Electromagnetic Theory (MMET)*, Lviv, 2016, pp. 337-340.
- [52] H. Ikuno, "Some remarks on Maxwell solvers for computational electromagnetics," *2003 IEEE Topical Conference on Wireless Communication Technology*, Honolulu, HI, USA, 2003, pp. 5-.
- [53] X. Min, W. Sun and K. M. Chen, "Stability analysis of the finite difference time domain method applied to unbounded electromagnetic problems," *International Symposium on Antennas and Propagation Society, Merging Technologies for the 90's*, Dallas, TX, USA, 1990, pp. 1640-1643 vol.4.
- [54] A. C. Lesina, A. Vaccari and A. Bozzoli, "A modified RC-FDTD algorithm for plasmonics in Drude dispersive media nanostructures," *2012 6th European Conference on Antennas and Propagation (EUCAP)*, Prague, 2012, pp. 687-690.
- [55] Z. Yang, Z. Lu, L. Wu, P. Zhang and M. Zhao, "A novel helical metamaterial absorber: Simulation study with the FDTD method," *2012 International Workshop on Metamaterials (Meta)*, Nanjing, 2012, pp. 1-3. doi: 10.1109/META.2012.6464961
- [56] Hai Lin, Ren-Sheng Dou, Gaofeng Wang and Bing-Zhong Wang, "FDTD-SUPML simulation of photonic integrated circuits," *2005 International Symposium on Electromagnetic Compatibility, 2005. EMC 2005.*, Chicago, IL, 2005, pp. 501-504 Vol. 2.

- [57] B. Westrick and A. Eroglu, "Improvement of FDTD simulation accuracy using the oversampling method of rasterization," Proceedings of the 2012 IEEE International Symposium on Antennas and Propagation, Chicago, IL, 2012, pp. 1-2.
- [58] (2019), 'Some Numerical Techniques for Maxwell's Equations in Different Types of Geometries', University of Colorado, CO 80309 [Online]. Available: <https://amath.colorado.edu/faculty/fornberg/Docs/forn.pdf>
- [59] (2019), 'Lumerical-Scripting Language', [Online]. Available: https://kb.lumerical.com/ref_scripts_scripting_language.html
- [60] (2019), 'Plane Wave Sources', [Online]. Available: https://kb.lumerical.com/ref_sim_obj_diffraction-plane-wave-source.html
- [61] (2019), 'Charge Transport (CT)', [Online]. Available: https://kb.lumerical.com/solvers_charge_transport.html
- [62] (2019), 'Modifying the Material Fits', [Online]. Available: https://kb.lumerical.com/materials_sampled_data_modify_fit.html
- [63] R.J. Collins, D.A. Kleinman, "Infrared reflectivity of zinc oxide," in *Journal of Physics and Chemistry of Solids*, vol. 11, pp. 190-194, 1959.
- [64] Anderson Janotti and Chris G Van de Walle, "Fundamentals of zinc oxide as a semiconductor", in *Reports on Progress on Physics*, vol. 71, 2009.
- [65] V. Srikant and D.R. Clake, "On the optical band gap of zinc oxide," in *Journal of Applied Physics*, vol. 83, Issue 10, 1998.
- [66] David C Look, "Electrical and optical properties of p-type ZnO," in *Semiconductor Science and Technology*, vol. 20, Number 4, 2005.
- [67] Jasprit Singh, 'Physics of semiconductors and their heterostructures', in *McGraw-Hill*, 1993.
- [68] Michael Schall and Peter Uhd Jepsen, "Above-band gap two-photon absorption and its influence on the ultrafast carrier dynamics in ZnTe and CdTe," in *Applied Physics Letters*, vol. 80, issue 25, 2002.
- [69] A. Dhar, D. Pradhan and J. N. Roy, " Nanostructures for highly efficient ultra-thin silicon solar cells," *2016 21st Century Energy Needs - Materials, Systems and Applications (ICTFCEN)*, Kharagpur, 2016, pp. 1-5.

- [70] Mihir Kumar Sahoo and Paresh Kale, "Integration of silicon nanowires in solar cell structure for efficiency enhancement: A review," in *Journal of Materiomics*, vol. 5, pp. 34-48, 2019.
- [71] X. Jiang, 'Aluminum-doped zinc oxide films as transparent conductive electrode for organic light-emitting devices,' in *Applied Physics Letters*, vol. 83, 2003.
- [72] Weiyan Wang, Quanyu Feng, Kemin Jiang, Jinhua Huang, Xianpeng Zhang, Weijie Song and Ruiqin Tan, "Dependence of aluminum-doped zinc oxide work function on surface cleaning method as studied by ultraviolet and X-ray photoelectron spectroscopies," in *Applied Surface Science*, vol. 257, pp. 3884-3887, 2011.
- [73] Songping Luo, Heping Shen, Xiaoli He, Ye Zhang, Jianbao Li, Dan Oron and Hong Lin, "Facile *in situ* synthesis of dendrite-like ZnO/ZnTe core/shell nanorod heterostructures for sensitized solar cells", in *Journal of Materials Chemistry C*, 2016.
- [74] Erik C. Garnett, Mark L. Brongersma, Yi Cui and Michael D. McGehee, "Nanowire Solar Cell", in *Annual Review of Materials Research*, vol. 41, p. 269-295, 2011.
- [75] Y. Hu *et al.*, "Cost-Efficient Formation of Flexible Pressure Sensor with Micropillar Arrays by Metal-Assisted Chemical Etching for Wearable Electronic Skin," *2018 IEEE 68th Electronic Components and Technology Conference (ECTC)*, San Diego, CA, 2018, pp. 790-795.
- [76] Jae Cheol Shin, Debashis Chanda *et al.*, " Experimental Study of Design Parameters in Silicon Micropillar Array Solar Cells Produced by Soft Lithography and Metal-Assisted Chemical Etching," in *IEEE Journal of Photovoltaics*, vol. 2, No. 2, 2012.
- [78] A. Ebong, M. Hilali, V. Upadhyaya, B. Rounsaville, I. Ebong and A. Rohatgi, "High-efficiency screen-printed planar solar cells on single crystalline silicon materials," *Conference Record of the Thirty-first IEEE Photovoltaic Specialists Conference, 2005.*, Lake Buena Vista, FL, USA, 2005, pp. 1173-1176.
- [79] Kwan Chi Kao, "3 - Optical and Electro-Optic Processes," in *Dielectric Phenomena in Solids*, pp. 115-212, 2004.
- [80] Yan He and Gang Ouyang, "Geometry-Dependent Auger Recombination Process in Semiconductor Nanostructures", in *Journal of Physical Chemistry*, 2017.

- [81] I. Magnusdottir, S. Bischoff, A. V. Uskov and J. Mørk, "Geometry dependence of Auger carrier capture rates into cone-shaped self-assembled quantum dots", in *Physical Review B*, vol. 67, 2003.
- [82] D.S. Meyaard, G.-B. Lin, J. Cho and E.F. Schubert, "9 - Efficiency droop in gallium indium nitride (GaInN)/gallium nitride (GaN) LEDs," in *Nitride Semiconductor Light-Emitting Diode (LEDS)*, pp. 279-300, 2014.
- [83] Rucksana Safa Sultana, Ali Newaz Bahar, Md. Asaduzzaman, Mohammad Maksudur Rahman Bhuiyan and Kawsar Ahmed, "Numerical dataset for analyzing the performance of a highly efficient ultrathin film CdTe solar cell," in *Data in Brief*, vol. 12, pp. 336-340, 2017.
- [84] Othmane Skhouni, R. Schrebler and Bernabe Mari Soucase, "ZnTe thin films grown by electrodeposition technique on Fluorine Tin Oxide substrates," in *Thin Solid Films*, 2014.
- [85] Vincent Consonni, Sebastien Renet and Jerome Garnier, "Improvement of the physical properties of ZnO/CdTe core-shell nanowire arrays by CdCl₂ heat treatment for solar cells," in *Nanoscale Research Letters*, v. 9(1), 2014. Doi: 10.1186/1556-276X-9-222.
- [86] Heayoung P. Yoon, Yu A. Yuwen, Chito E. Kendrick and Greg D. Barbe, "Enhanced conversion efficiencies for pillar array solar cells fabricated from crystalline silicon with short minority carrier diffusion lengths," in *Applied Physics Letters*, vol. 96, 2010.
- [87] Junshuai Li, Hong Yu Yu and Yali Li, "Solar energy harnessing in hexagonally arranged Si nanowire arrays and effects of array symmetry on optical characteristics," in *Nanotechnology*, 2011.
- [88] M. Zeman *et al.*, "High-Efficiency Crystalline Silicon Solar Cell Architectures," *2018 12th International Conference on Advanced Semiconductor Devices and Microsystems (ASDAM)*, Smolenice, 2018, pp. 1-6.
- [89] J. Li, HongYu Yu, She Mein Wong, Gang Zhang, Guo-Qiang Lo and Dim-Lee Kwong, "Surface nanostructure optimization for solar energy harvesting in Si thin film based solar cells," *2009 IEEE International Electron Devices Meeting (IEDM)*, Baltimore, MD, 2009, pp. 1-4.